Journal of Nanobiotechnology

RESEARCH Open Access

Exosome-like vesicles encapsulated with specific microRNAs accelerate burn wound healing and ameliorate scarring

Zhiyong Lei[1,3], Xiaojuan Chen[1,3], Kezhuo Chen[1,3], Pan Liu[1], Mingzhang Ao[1], Lu Gan[2] and Longjiang Yu[1,3*]

Abstract

Burn injuries are prevalent, yet effective treatments remain elusive. Exosomes derived from mesenchymal stem cells (MSC-Ex) possess remarkable pro-regenerative properties for wound healing. Despite their potential, the challenge of mass production limits their clinical application. To address this, preparing exosome-like vesicles has become an international trend. In this study, 28 key microRNAs (miRNAs) with significant pro-proliferation, anti-inflammation, and anti-fibrosis functions were screened from MSC-Ex. These miRNAs were encapsulated into liposomes and then hybridized with extracellular vesicles derived from watermelon to create synthetic exosome-like vesicles. The fabricated vesicles exhibited similar particle size and zeta potential to MSC-Ex, demonstrating high serum stability and effectively resisting the degradation of miRNA by RNase. They were efficiently internalized by cells and enabled a high rate of lysosomal escape for miRNAs post cellular uptake, thereby effectively exerting their pro-proliferative, anti-inflammatory, and anti-fibrotic functions. Further experiments demonstrated that these vesicles efficiently accelerated burn wound healing and reduced scarring, with effects comparable to those of natural MSC-Ex. Based on these findings, the exosome-like vesicles fabricated in this study present a promising alternative to MSC-Ex in burn wound treatment.

*Correspondence:
Longjiang Yu
yulongjiang@hust.edu.cn

Full list of author information is available at the end of the article

Graphical Abstract

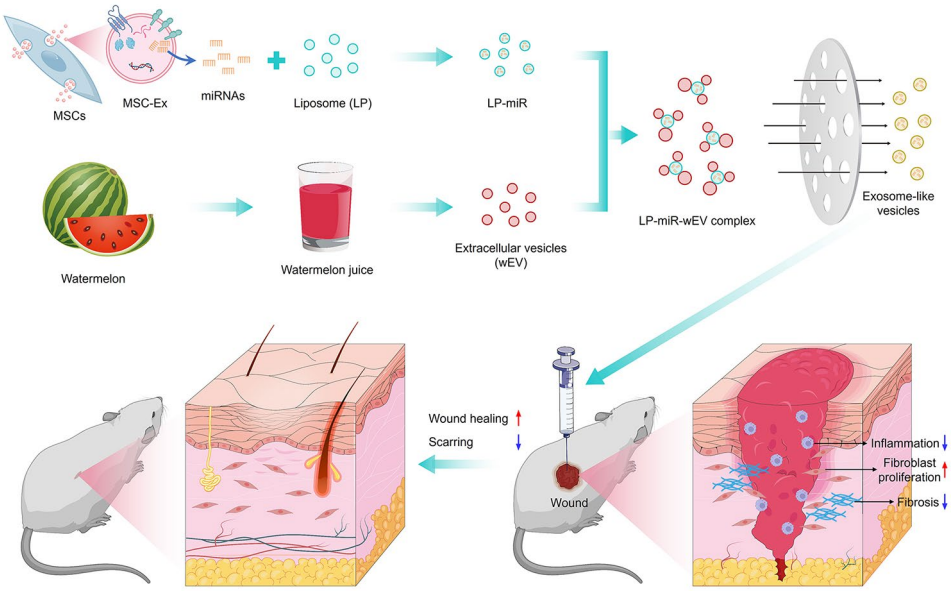

Keywords microRNA, Exosome-like vesicles, Mesenchymal stem cells, Exosomes, Wound, Scar

Introduction

Burn injuries pose a great threat to people's physical health and economic development. In 2019, approximately 9 million new cases of burn injuries were recorded globally, resulting in an estimated 111,000 deaths and contributing to annual welfare losses of up to 112 billion USD [1]. Burn wounds are often accompanied by severe inflammation, characterized by a protracted healing process and a high propensity for the development of hypertrophic scars, making them one of the most challenging types of cutaneous wounds to manage clinically [2]. To date, there are no clinically effective therapies for the treatment of burn wounds. To overcome these challenges and enhance patient outcomes, the development of cost-effective and efficient treatments is imperative.

The discovery of mesenchymal stem cells (MSCs) and their secreted exosomes (MSC-Ex) has brought a new dawn to this field. After skin injury, MSCs are chemotactically driven to migrate from their niches to the wound site. Upon encountering specific stimuli from the microenvironment, MSCs secrete a range of cytokines tailored to the demands of the wound site, including those that promote proliferation, exhibit anti-inflammatory properties, and prevent fibrosis, primarily via exosomes [3, 4]. This targeted secretion modulates the behavior of multiple cell types within the wound tissue, culminating in rapid and scar-minimizing wound healing. A number of studies have demonstrated that MSC-Ex are more suitable for wound treatment compared to the MSCs themselves [5, 6]. However, current production of MSC-Ex is limited to small-scale laboratory settings, and scaling up to meet clinical and commercial demands remains elusive. The production of MSC-Ex is reliant on cell culture, resulting in challenges such as limited scalability, time and cost constraints, poor batch-to-batch uniformity, and difficulties in quality control [7–9]. Due to the challenges associated with the mass production of natural MSC-Ex, the preparation of synthetic exosome-like vesicles is increasingly emerging [10–12].

In pursuit of this goal, selecting the critical bioactive components within MSC-Ex and the development of nanovesicles that emulate the structure and characteristics of MSC-Ex are two critical issues in the preparation of exosome-like vesicles. Exosomes contain a variety of active ingredients, such as proteins, miRNAs, mRNAs, and lncRNAs. miRNAs, which comprise a significant portion of the active constituents, regulate a vast array of physiological processes and are simple and inexpensive to produce [13–15]. Meanwhile, a single miRNA possesses the capability to modulate the translation processes of multiple target mRNAs, thereby exerting regulatory influence over multiple signaling pathways [16, 17]. It has been proven that miRNAs exert pivotal roles in the processes of tissue regeneration, including but not limited to cutaneous, osseous, and neural systems [18–20]. Based on these, miRNAs are ideal for industrial production to mimic the functions of MSC-Ex in wound healing. As previously reported, exosomes contain hundreds

of distinct miRNAs [21, 22]. However, the precise functions of a significant proportion of the MSC-Ex-derived miRNAs remain unknown. Consequently, screening miRNAs from MSC-Ex that specifically facilitate wound healing remains challenging.

In this study, a function-oriented miRNA sequencing approach was applied to select miRNAs within MSC-Ex that are specifically beneficial for cutaneous wound repair, resulting in the screening of 32 candidate miRNAs. Functional assays showed that among these 32 miRNAs, 15 significantly promoted the proliferation of dermal fibroblasts, while all exhibited anti-inflammatory and anti-fibrotic capabilities. Based on the results of functional assays, 28 miRNAs that primarily exhibit pro-proliferative, anti-inflammatory, and anti-fibrotic effects were chosen for subsequent studies. To ensure the efficacious uptake of miRNAs by recipient cells and their optimal functionality, novel exosome-like vesicles mimicking the characteristics of MSC-Ex have been fabricated to deliver the 28 miRNAs. First, watermelon-derived extracellular vesicles were prepared and exhibited excellent biosafety as well as significant pro-proliferative efficacy on dermal fibroblasts. Then, the watermelon-derived extracellular vesicles were hybridized with miRNA-loaded liposomes, resulting in exosome-like vesicles that possess characteristics similar to those of natural MSC-Ex. These exosome-like vesicles enabled the miRNAs to have a high lysosomal escape rate upon entering cells, efficiently performing their regulatory functions. In vivo experiments confirmed that, similar to natural MSC-Ex, they effectively promoted wound healing and mitigated scar formation in deep second-degree burn wounds. Thereby, the exosome-like vesicles provide a mass-producible, cost-effective, and efficient substitute to MSC-Ex.

Results and discussion

Inflammatory microenvironment-educated MSCs produce exosomes with enhanced regenerative potential in burn wounds

To screen the pro-regenerative miRNAs from MSC-Ex, we aimed to specifically enhance the reparative properties of MSC-Ex. Following this, miRNA sequencing will be applied to assess the miRNA composition and relative expression levels of each miRNA between the functionally enhanced and regular MSC-Ex. This function-oriented miRNA sequencing approach is supposed to aid in screening the key miRNAs that promote wound healing within MSC-Ex.

Previous studies have reported that MSCs can adjust the composition and functionality of their secreted exosomes in response to the distinct microenvironments in which they reside [23]. Herein, macrophages were induced by lipopolysaccharide (LPS) to undergo a transition to an inflammatory state (Figure S1). Subsequently, the culture medium containing the secreted products from these inflammatory macrophages was collected and concentrated (Fig. 1A), designated as CCM. To mimic the inflammatory microenvironment that MSCs may encounter when migrating into the wound tissue and to enhance the pro-regenerative function of their secreted exosomes, MSCs were educated with varying concentrations of CCM. It was shown that MSCs exposed to 10% and 5% CCM (designated MSC_{10} and MSC_5) displayed abnormal morphology and suppressed proliferation (Fig. 1B, C and Fig. S2) as compared with the control MSCs (MSC_0), consistent with literature findings [24, 25]. Additionally, we made the initial discovery that MSCs exposed to 1.25% CCM (named $MSC_{1.25}$) exhibited enhanced proliferative capability (Fig. 1B, C). Then, MSC-Ex were prepared from the medium via ultracentrifugation. They were characterized as having a standard size distribution (30–130 nm) and exhibiting typical exosomal markers of CD9 and CD81 (Fig. 1D-F).

Promoting the proliferation of skin cells, reducing inflammatory responses, and preventing fibrogenesis are common strategies for accelerating wound healing and preventing scar formation [26]. Functional assays revealed significant disparities in pro-proliferative, anti-inflammatory, and anti-fibrotic efficacy among exosomes secreted by MSCs stimulated with CCM at concentrations of 10%, 5%, 2.5%, 1.25%, and 0%, respectively (named EX_{10}, EX_5, $EX_{2.5}$, $EX_{1.25}$, and EX_0). In the CCK-8 assay (Fig. 2A), $EX_{1.25}$ exhibited significantly enhanced (139.07 ± 5.65%) activity in promoting the proliferation of mouse dermal fibroblasts compared to EX_0 (118.14 ± 8.09%), while EX_{10} and EX_5 had no significant effect on the proliferation of cells. Similarly, cells treated with $EX_{1.25}$ exhibited the highest PCNA expression (Fig. 2B), indicating the greatest proliferative capacity. The in vitro anti-inflammatory assays (Fig. 2C) demonstrated that all five groups of exosomes significantly inhibited the nitric oxide (NO) synthesis in macrophages induced by LPS, when compared with the negative control (NC) group. Notably, macrophages treated with $EX_{1.25}$ showed the lowest levels of NO synthesis (0.64-fold of NO expression vs. EX_0 group). Western blotting analysis of nitric oxide synthase 2 (NOS2) expression (Fig. 2D) in macrophages of various groups demonstrated similar results. To further validate this conclusion, the levels of inflammatory cytokines interleukin-1 beta (IL-1β) and tumor necrosis factor-alpha (TNF-α) in the supernatants of various cell groups were also measured (Figure S3), with results consistent with those depicted in Fig. 2C and D. Upon stimulation with transforming growth factor-beta 1 (TGF-β1), dermal fibroblasts undergo polarization, leading to the substantial synthesis of α-smooth muscle actin (α-SMA) and the induction

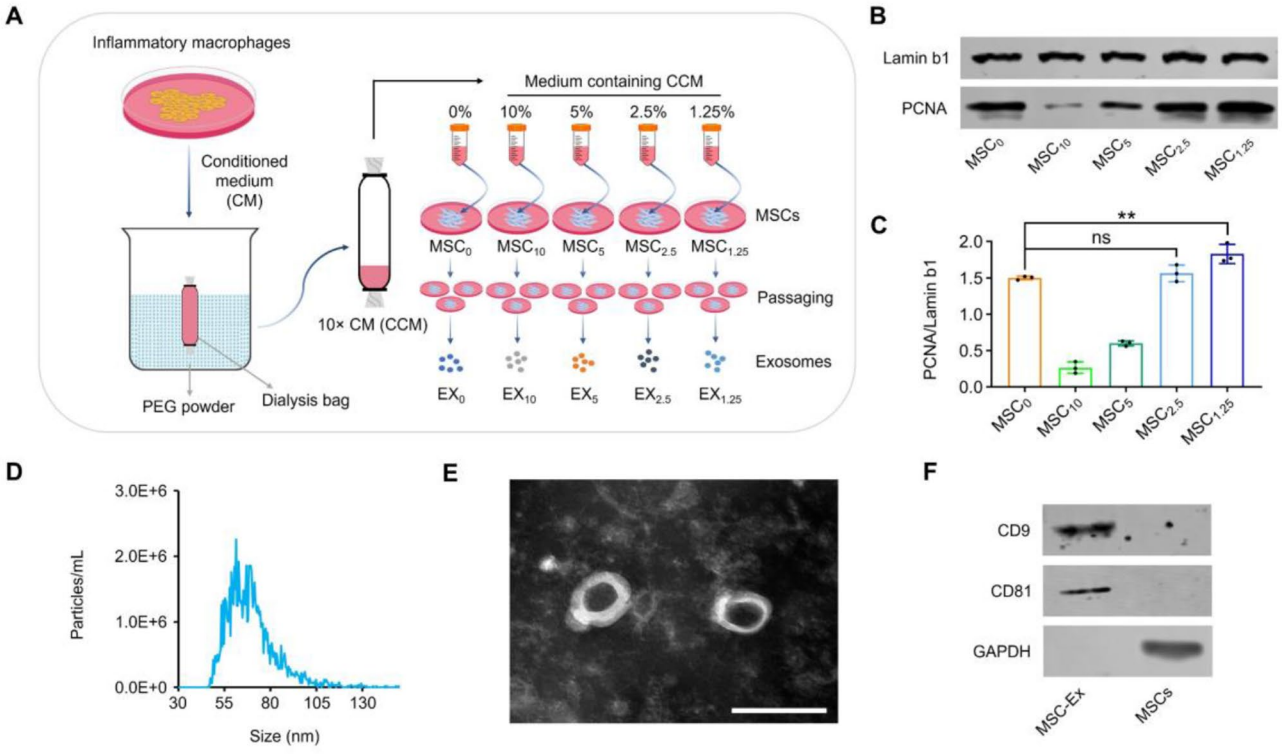

Fig. 1 The induction of MSCs and the identification of exosomes. (**A**) Schematic diagram of MSCs induction. (**B**,**C**) Western blotting and quantitative analysis of proliferating cell nuclear antigen (PCNA, a marker of cell proliferation) in MSCs, with "Lamin b1" as the loading control. Statistical analysis was performed by one-way ANOVA with Tukey's multiple comparison test, $^{**}P < 0.01$, ns, not significant. Data are presented as mean ± S.D. (**D**) Size distribution of MSC-Ex. (**E**) Representative images of transmission electron microscopy (TEM) analysis of MSC-Ex. Scale bar: 100 nm. (**F**) Western blotting analysis of surface markers (CD9 and CD81) of MSC-Ex

of tissue fibrosis, which results in scar formation [3, 4]. The in vitro gel contraction assay is a classical and effective method for evaluating the degree of fibroblast polarization. It was demonstrated that all groups of MSC-Ex significantly inhibited the TGF-β1-induced gel contraction capacity of fibroblasts, with the $EX_{1.25}$ treated group showing the lowest rate of contraction (Fig. 2E, F). Western blotting analysis of α-SMA further indicated that $EX_{1.25}$ exhibited the strongest antagonistic effect on TGF-β1-induced α-SMA synthesis (Fig. 2G). These results demonstrated that $EX_{1.25}$ possess the best proliferative, anti-inflammatory, and anti-fibrotic functions among the five groups of MSC-Ex; meanwhile, the stimulus intensity of the inflammatory environment determines the ultimate functional orientation of MSC-Ex. Based on this, subsequent research will focus on EX_0 and $EX_{1.25}$.

The deep second-degree burn wound model was established in mice to compare the in vivo wound healing and anti-scarring activities of $EX_{1.25}$ and EX_0. Compared with the control group, both $EX_{1.25}$ and EX_0 significantly promoted burn wound healing and mitigated scar formation (Fig. 2H). Additionally, the $EX_{1.25}$ group demonstrated a stronger wound healing capability than the EX_0 group, along with a reduction in scarring. On day 6, the percentage of the remaining wound area in the $EX_{1.25}$ group and the EX_0 group was 40.16 ± 5.44% and 54.31 ± 13.14% (Fig. 2I), respectively. By day 9, these values decreased to 9.47 ± 6.39% and 23.01 ± 10.61% in the $EX_{1.25}$ group

and the EX_0 group, respectively. The results of H&E staining (Fig. 2J) revealed that on day 6, both the EX_0 and $EX_{1.25}$ groups showed greater granulation tissue formation at the wound sites compared to the control group, with the $EX_{1.25}$ group exhibiting superior granulation tissue development than the EX_0 group. In the subsequent healing process, compared to the control group, both the EX_0 and $EX_{1.25}$ groups showed a faster extracellular matrix formation. Furthermore, by day 18, wounds treated with $EX_{1.25}$ demonstrated enhanced regeneration of cutaneous appendages, such as hair follicles and sweat glands (marked with blue arrows), compared to wounds treated with EX_0. These results indicate that $EX_{1.25}$ possess a superior pro-regenerative capacity for wound healing over EX_0.

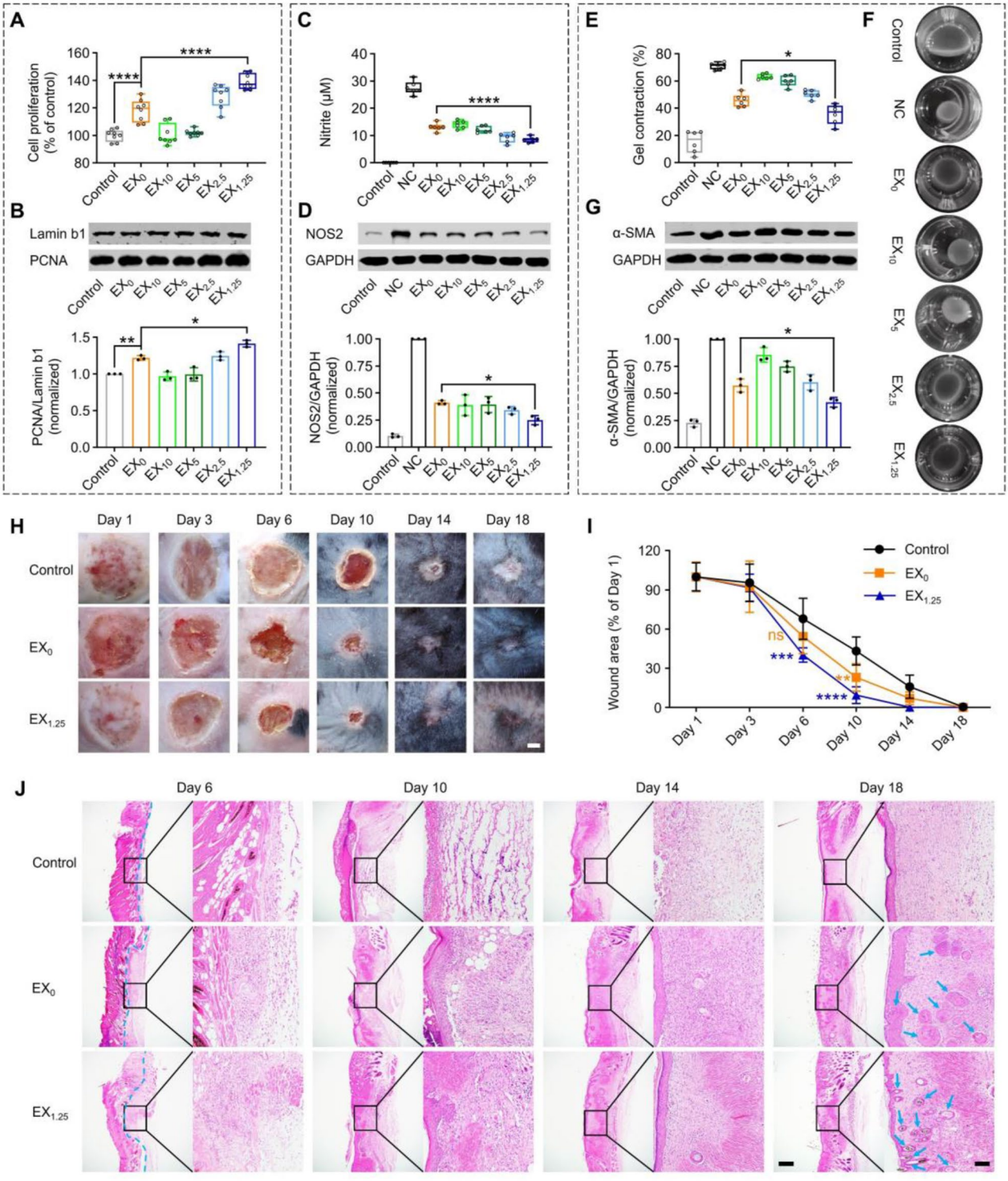

Fig. 2 (See legend on next page.)

(See figure on previous page.)

Fig. 2 Comparison of the biological functions of EX_0, EX_{10}, EX_5, $EX_{2.5}$, and $EX_{1.25}$. The CCK-8 assay (**A**) and the western blotting analysis of PCNA (**B**) were carried out to evaluate the pro-proliferative effect of EX_0, EX_{10}, EX_5, $EX_{2.5}$, and $EX_{1.25}$ on dermal fibroblasts. The effects of the five groups of MSC-Ex on the LPS-induced inflammatory response were assessed. NO (evaluated by nitrite content) synthesis (**C**) and relative expression of NOS2 (**D**) in macrophages were tested, with GAPDH as the loading control. Gel contraction assay (**E**, **F**) and western blotting analysis (**G**) were performed to compare the anti-fibrotic effect of the five groups of MSC-Ex on TGF-β1-activated dermal fibroblasts. Higher gel contraction percentages (**E**) or smaller collagen matrices (**F**) indicate stronger fibrogenesis. For western blotting analysis (**G**) of α-SMA (a marker of fibrosis) in TGF-β1-treated dermal fibroblasts, the higher α-SMA expression suggests a higher fibrotic level. In vivo pro-regenerative effects of EX_0 and $EX_{1.25}$ were compared. (**H**) Photographs of representative wounds from each group on different post-wound days. Scale bar: 2 mm. (**I**) Quantification of the residual wounds; significance was compared with the control group. (**J**) Photomicrography of wounds (H&E staining). In the images of the wound tissue on Day 6, the necrotic tissue is on the left side of the blue dashed line, while the regenerated tissue is on the right side of the blue dashed line. Scale bars: 200 μm (left) or 50 μm (right). All statistical analyses were performed by one-way ANOVA with Tukey's multiple comparison test, $^*P<0.05$, $^{**}P<0.01$, $^{***}P<0.001$, $^{****}P<0.0001$, ns, not significant. Data are presented as mean ± S.D

The miRNAs derived from MSC-Ex have significant pro-proliferative, anti-inflammatory, and anti-fibrotic abilities

To pinpoint the key miRNAs exerting pro-regenerative effects within MSC-Ex, miRNA sequencing was conducted on the miRNAs within EX_0 and $EX_{1.25}$. The study revealed that a total of 682 miRNAs were expressed across the two groups of exosomes (Fig. 3A and Table S1). Significant differences were observed in the relative abundance of many miRNAs between the groups (Fig. 3B, C). In comparison to EX_0, $EX_{1.25}$ exhibited a significant upregulation of 40 miRNAs and a significant downregulation of 77 miRNAs. Given that $EX_{1.25}$ demonstrated a higher pro-regenerative capacity compared to EX_0, the miRNAs that play a primary role should be more abundant in $EX_{1.25}$ or exhibit high abundance in both exosome groups. Oriented by this principle, 32 miRNAs were pre-screened for further exploration (Table S2), including four novel miRNAs (2_18240, 3_21147, 5_24979, and 6_26497). The 32 miRNAs accounted for 84.05% and 79.92% (Fig. 3D) of total miRNAs in $EX_{1.25}$ and EX_0, respectively.

The study of miRNAs has emerged in recent years, and the functions of many miRNAs have not yet been well determined. Herein, functional studies were performed on the pre-screened 32 miRNAs. The CCK-8 assay showed that 15 of these miRNAs promoted the proliferation of dermal fibroblasts (Fig. 4A). This conclusion was further substantiated by western blotting analysis, with cells transfected with these 15 miRNAs exhibiting elevated levels of PCNA expression (Figure S4). To the best of our knowledge, the pro-proliferative effect of the majority of these miRNAs on skin cells was first identified, excluding miR-145a-5p, miR-21a-5p, miR-24-3p, and miR-92a-3p. The results of the anti-inflammatory assays demonstrated that the 32 miRNAs were capable of suppressing the LPS-induced inflammatory phenotype transition in macrophages to varying extents. In comparison with the NC group, the experimental groups

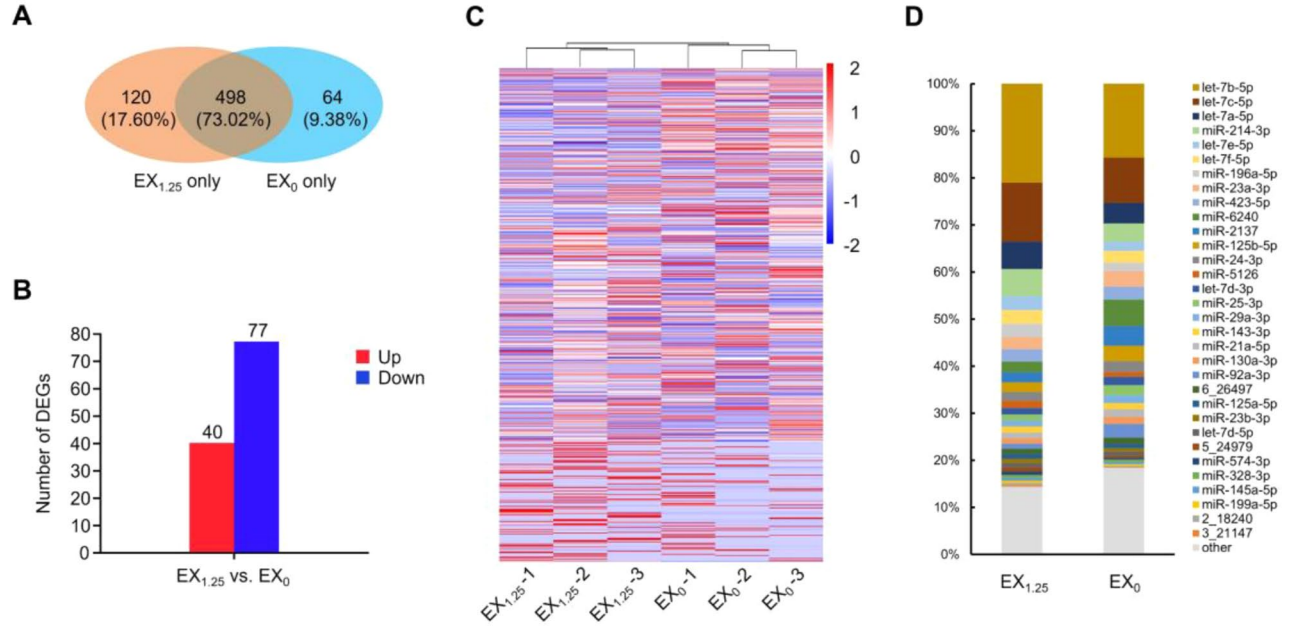

Fig. 3 The differential expression of miRNAs between $EX_{1.25}$ and EX_0. (**A**) Differences in miRNA composition between $EX_{1.25}$ and EX_0. (**B**) The number of differentially expressed miRNAs in $EX_{1.25}$ and EX_0. (**C**) The clustering heatmap of differentially expressed miRNAs in $EX_{1.25}$ and EX_0. (**D**) Percentage distribution of the 32 miRNAs screened in $EX_{1.25}$ and EX_0

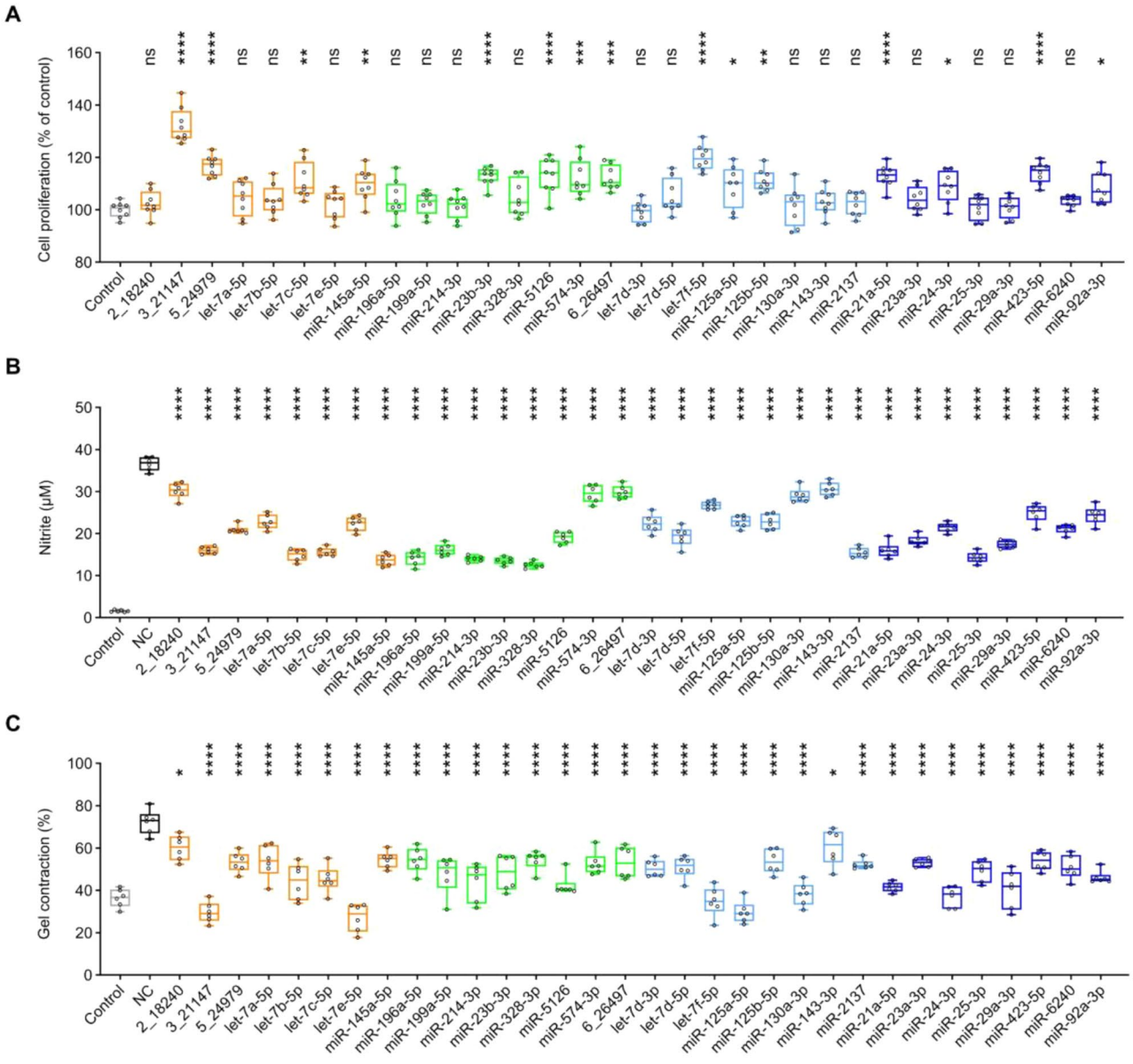

Fig. 4 Effects of the 32 miRNAs on dermal fibroblast proliferation, LPS-induced inflammatory responses, and TGF-β1-driven fibrosis. (**A**) Results of the CCK-8 assay. (**B**) NO synthesis of macrophages. (**C**) Results of the gel contraction assay. All statistical analyses were performed by one-way ANOVA with Tukey's multiple comparison test. For (**A**), significance was compared with the control group; for (**B**) and (**C**), significance was compared with the NC group. *$P < 0.05$, **$P < 0.01$, ***$P < 0.001$, ****$P < 0.0001$, ns, not significant. Data are presented as mean ± S.D

transfected with these miRNAs displayed significantly reduced expression levels of NO (Fig. 4B) and NOS2 (Figure S5). The assessment of inflammatory cytokines IL-1β and TNF-α (Figure S6) in the supernatants of various cell groups also yielded concordant findings. Notably, 2_18240, miR-574-3p, 6_26497, miR-130a-3p, and miR-143-3p demonstrate relatively weaker anti-inflammatory capabilities compared to other miRNAs. The results from the gel contraction assay (Fig. 4C and Figure S7) indicate that all miRNAs possess a certain degree of anti-fibrotic capability, with 3_21147, let-7e-5p, and miR-125a-5p demonstrating particularly prominent (gel contraction % < 30) anti-fibrotic effects among the 32 miRNAs tested. These results were further corroborated by western blotting analysis, and the findings from both assays were largely consistent (Figure S8). The anti-inflammatory and anti-fibrotic functions of several miRNAs (2_18240, 3_21147, 5_24979, 6_26497, miR-5126, let-7d-3p, miR-2137, and miR-6240) were reported for the first time globally.

Given the results presented above, four miRNAs (2_18240, miR-574-3p, 6_26497, and miR-143-3p) will be excluded from subsequent studies. These miRNAs demonstrated slight anti-inflammatory capabilities and

unimpressive anti-fibrotic effects; furthermore, 2_18240 and miR-143-3p specifically lacked the capacity to enhance the proliferation of dermal fibroblasts.

To better elucidate how the final-screened 28 miRNAs exert their functions in promoting proliferation, anti-inflammation, and anti-fibrogenesis, in silico analysis was conducted to identify the targets of these miRNAs. The signaling pathways commonly targeted for macrophage-directed therapies in clinical applications have been well defined [27]. The results of in silico analysis suggested that the 28 miRNAs can downregulate the expression of most signaling proteins within these pathways (Figure S9), such as the TLR, TNF, and IFN pathways, thereby mitigating inflammatory responses. Similarly, the classic fibrosis-associated signaling pathways, such as the TGF-β1/SMAD and the Wnt/β-Catenin pathways, are intensively regulated by these miRNAs (Figure S10). miRNAs with pro-proliferative functions typically exert their effects by downregulating the expression of proteins that possess anti-proliferative or pro-apoptotic activities [28, 29]. Several miRNAs are supposed to target the signaling proteins that have an inhibitory effect on cell proliferation, such as the p53/p21 signaling pathway (Figure S10). It should be noted that only well-recognized signaling pathways are depicted in Figures S9 and S10, with many other less-established related signaling pathways not being listed. Consequently, some miRNAs that are not shown may exert their regulatory effects through other signaling pathways.

The healing process of wounds is extremely complex, and the understanding of this process is still far from adequate. As is currently known, the repair process involves multiple signaling pathways [30, 31], Given the intricacies of dermal architecture and the inherent reparative mechanisms of wound healing, the modulatory capacity of individual bioactive constituents is typically confined to a limited array of signal transduction pathways and cellular behaviors [32, 33]. The extensive regulatory influence exerted by these 28 miRNAs on the wound healing process underscores their formidable potential for therapeutic exploitation. This suggests that the combined action of these miRNAs may offer advantages over traditional therapeutics.

The synthetic exosome-like vesicles display similar characteristics to natural MSC-Ex

miRNAs are vulnerable to degradation by ubiquitous ribonucleases, and free miRNAs are seldom internalized by cells [34]. Therefore, it is essential to develop a nanocarrier with high encapsulation efficiency for miRNAs and excellent resistance to RNase degradation to deliver miRNAs into cells. Furthermore, after the cells have engulfed the nanocarriers loaded with miRNAs, it is crucial for the miRNAs to be successfully released from the lysosomes, enter the cytoplasm, bind to mRNAs, and thus exert their regulatory effects on cellular behavior.

Previous studies have shown that exosomes can be effectively internalized by cells, with a high lysosomal escape rate for the loaded cargos [35, 36]. To ensure efficient cellular uptake and a high lysosomal escape rate of miRNAs, developing a novel nanocarrier that mimics natural exosomes is a promising direction. In recent years, plant-derived extracellular vesicles have been demonstrated as a novel and promising type of nanoscale drug delivery vehicle. They possess structural features similar to those of animal-derived exosomes, exhibit good biocompatibility, and are more cost-effective and have a significantly higher production yield compared to animal-derived exosomes [37, 38]. Watermelon, which is not only inexpensive and readily available but also has extracts that have been proven to possess certain anti-inflammatory and wound healing properties [39, 40], can serve as an ideal source of plant-derived extracellular vesicles. Herein, extracellular vesicles derived from watermelon were isolated and designated as wEV. The average hydrated particle size of wEV was shown to be 55.27 nm, and it was demonstrated that they carry a negative charge (Fig. 5A, B). In our experiment, 23.87 ± 2.63 mg of wEV (mass of protein) were obtained per liter of watermelon juice. In vitro assays demonstrated that wEV significantly enhanced the proliferation of dermal fibroblasts (Fig. 5C-E), exhibiting a clear concentration-dependent effect. Furthermore, wEV exhibited excellent immunocompatibility and did not induce macrophages to polarize towards an inflammatory state (Fig. 5F-H and Figure S11). On the contrary, they can inhibit the inflammatory polarization of macrophages triggered by LPS. Next, we found that wEV did not induce fibroblasts to transition towards a pro-fibrotic phenotype and exhibited no significant promoting or inhibitory effects on fibrosis induced by TGF-β1 (Figure S12).

To clarify the material basis underlying the functions of wEV in promoting proliferation and exerting anti-inflammatory effects, a metabolomics analysis was performed. The results showed that wEV contain a total of 2,991 substances (Table S3). Among these substances, there are 683 amino acids and derivatives, 112 nucleotides and derivatives, 377 terpenoids, 331 lipids, 327 alkaloids, 228 flavonoids, 197 phenolic acids, and 124 organic acids (Fig. 5I). In addition, wEV also contain other bioactive substances, such as lignans and coumarins. Among these substances, amino acids and derivatives have the highest relative content, accounting for 37.69% of the total substances (Fig. 5J). Alkaloids, lipids, and nucleotides and derivatives account for 16.55%, 13.26%, and 8.4% of the total substances, respectively. The proportions of other substances are relatively lower. Further analysis revealed that wEV contain 14 types of coding amino

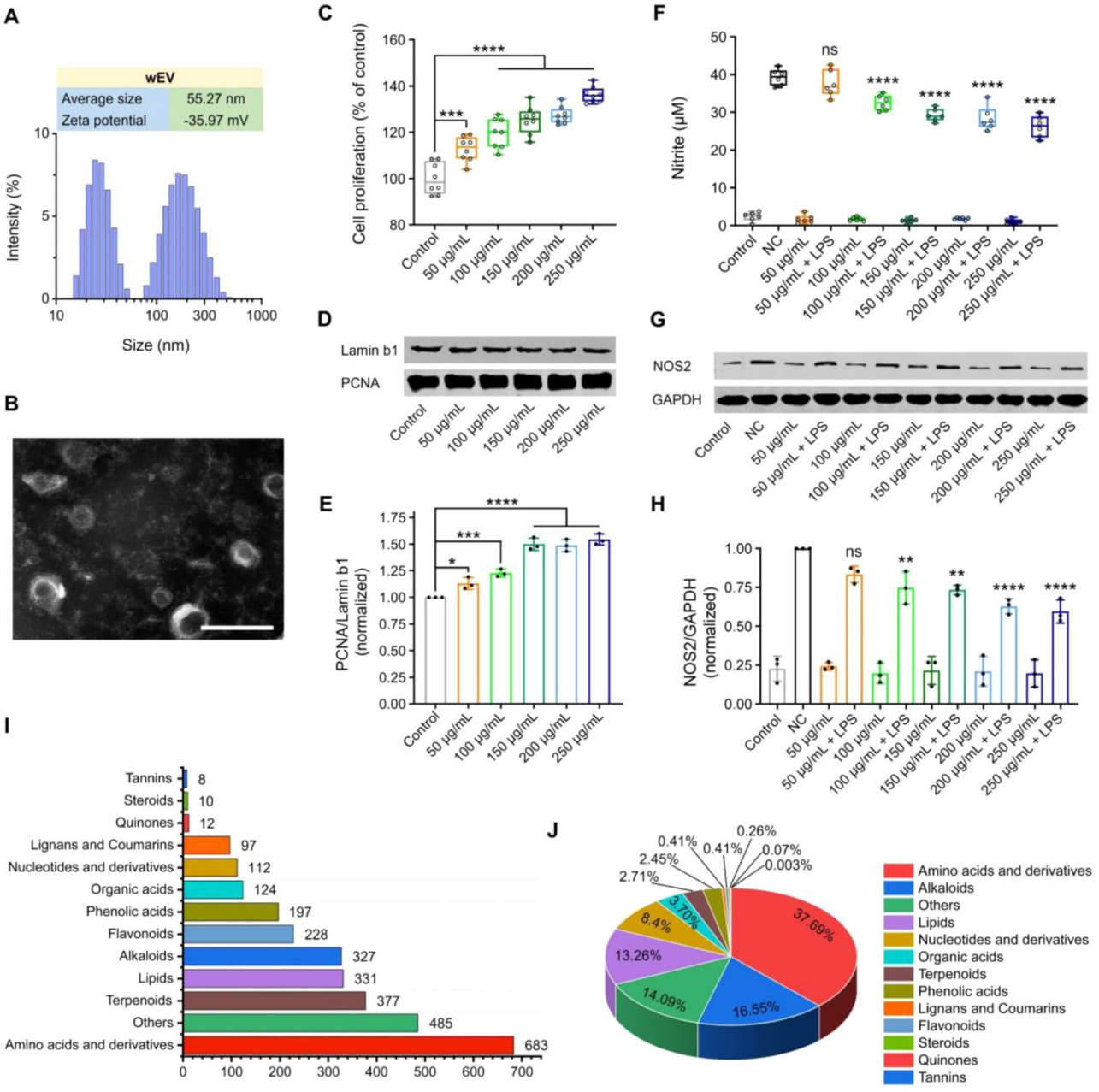

Fig. 5 Characterization, biological functions, and metabolomics analysis of wEV. (**A**) Hydrated particle size and zeta potential of wEV. (**B**) Representative images of TEM analysis of wEV. (**C-E**) The effects of wEV on dermal fibroblast proliferation. (**C**) Results of the CCK-8 assay. (**D**, **E**) Western blotting and quantification of PCNA in dermal fibroblasts treated with various concentrations of wEV. (**F-H**) Effects of wEV on LPS-induced inflammation and whether wEV induces the transition of macrophages to an inflammatory state. (**F**) Concentration of NO (evaluated by nitrite content) in the culture medium of macrophages. (**G**, **H**) Western blotting and quantification of NOS2 expression in macrophages after treatment with LPS. (**I**, **J**) Metabolomics analysis results of wEV. (**I**) Number of various small molecule substances in wEV. (**J**) Percentage content of various small molecule substances in wEV. All statistical analyses were performed by one-way ANOVA with Tukey's multiple comparison test. $^{*}P < 0.05$, $^{**}P < 0.01$, $^{***}P < 0.001$, $^{****}P < 0.0001$, ns, not significant. Data are presented as mean ± S.D. For (**F**) and (**H**), significance was compared with the NC group

acids and various amino acid derivatives (which can be processed into amino acids after entering cells), providing raw materials for protein synthesis. In addition, wEV contain various deoxynucleosides and nucleosides, which serve as direct raw materials for the synthesis of DNA and RNA. They also contain cAMP, cGMP, and tetrahydrofolate, which can indirectly promote the synthesis of DNA and RNA. Moreover, lysophosphatidylcholine, lysophosphatidylethanolamine, sphingosine, ceramide, oleic acid, linoleic acid, and their derivatives in wEV play important roles in the formation, maintenance, and functioning of cell membranes [41]. Based on these

findings, we speculate that wEV may promote cell proliferation by facilitating the generation of cellular DNA, RNA, proteins, and membrane structures. As for the anti-inflammatory effects, wEV contain a variety of bioactive substances such as alkaloids, terpenoids, and flavonoids, which possess anti-inflammatory properties. This may serve as the material basis for its anti-inflammatory effects.

The above results indicate that wEV can not only be regarded as a very promising drug delivery vehicle, but its inherent "supply effect" on cell proliferation and its role in inflammation regulation are also highly beneficial for wound healing. However, current methodologies for the encapsulation of drugs within plant-derived extracellular vesicles have yielded unsatisfactory encapsulation efficiencies (such as electroporation, extrusion, and ultrasonication), particularly for large molecular-weight therapeutics [42]. To address this issue, we attempted to fuse liposomes with wEV for the development of hybrid liposome-wEV nanoplatforms to load miRNA. In recent years, researchers have found that these hybrid carriers, obtained by fusing liposomes with animal/plant-derived vesicles, not only retain the advantages of both nanocarriers but also avoid their respective shortcomings [43]. Herein, liposomes (LP) formulated with DC-Cholesterol and Dioleoyl Phosphatidylethanolamine were prepared, and subsequently loaded with miRNA mimics, yielding LP-miR. Then, LP-miR was hybridized with wEV, resulting in exosome-like vesicles (LPEx), with particle sizes and zeta potentials that closely resemble those of natural exosomes. Both MSC-Ex and LPEx exhibited hydrated particle sizes around 130 nm (Fig. 6A) with a relatively narrow distribution range [44, 45]; additionally, their zeta potentials were closely aligned. The hydrated particle size of LP was measured at 160.97 nm, and they carried a substantial positive charge. The particle sizes of these nanocarriers were further confirmed by TEM analysis (Fig. 6B).

A comparative analysis of miRNA encapsulation efficiency among LP, LPEx, and wEV revealed that both LP and LPEx exhibited high miRNA encapsulation rates, amounting to 99.15 ± 0.53% and 94.94 ± 2.58%, respectively (Fig. 6C). Conversely, wEV demonstrated a markedly low miRNA encapsulation efficiency [46], recorded at merely 6.78 ± 1.63%. Serum stability tests revealed that the unloaded LP (positively charged) were likely to adsorb the proteins (negatively charged) in exosome-free serum and form a liposome–protein corona (Figure S13), resulting in larger particles (1121.00 nm) and acquiring a negative charge [47, 48]. In contrast, the particle size of miRNA-loaded LP (LP-miR) increased slightly upon serum addition. miRNAs adsorbed on the surface of LP may provide a certain degree of steric hindrance, limiting the adsorption of LP to proteins in serum. LPEx and wEV, both of which are negatively charged, exhibited high stability in serum. Their particle size remained largely unchanged. However, a slight decrease in zeta potential was observed. This suggests that LPEx and wEV may not undergo significant adsorption in serum, indicating excellent serum

stability. Meanwhile, the particle size and zeta potential of LPEx and wEV treated with trypsin significantly decreased, indicating that the surface proteins of these nanovesicles may have been degraded. This further suggests that LPEx and wEV exhibit high stability in serum, with serum enzymes only capable of causing slight degradation to their surface proteins. Following that, we investigated the resistance to RNase degradation of miRNA encapsulated by LPEx. Results show that free miRNA was completely degraded when exposed to RNase A, whereas miRNA encapsulated within LPEx showed non-significant degradation (Figure S14).

Cytotoxicity is one of the non-negligible aspects of nanomedicine. Both CCK-8 assay and live/dead cell fluorescence staining results indicate that LP generated significant cytotoxicity on dermal fibroblasts and macrophages (Fig. 6D-G and Figure S15). The positively charged surface of liposomes can disrupt the cell membrane, resulting in cytotoxicity [49], which explains why LP exhibited significant cytotoxicity to dermal fibroblasts and macrophages. In contrast, LPEx and wEV exerted a significant enhancement effect on dermal fibroblast proliferation (Fig. 6D), the results of live/dead cell fluorescence staining also indicated that LPEx and wEV did not lead to cell death (Fig. 6F, G). Notably, wEV but not LPEx demonstrated a slight attenuating effect on cell proliferation to macrophages (Fig. 6E), while no significant elevated cell death was found (Figure S15). This could be one of the mechanisms through which wEV exert their anti-inflammatory function.

miRNAs encapsulated in LPEx efficiently perform their biological functions

To assess the delivery efficiency of miRNAs using LPEx, the cellular uptake kinetics of LP, LPEx, and wEV were compared. The results (Figure S16) showed that the uptake of LP, LPEx, and wEV by cells increased with the incubation time. However, for both dermal fibroblasts and macrophages, the uptake of LPEx was higher than that of LP, while the lowest uptake was observed for wEV, which may be attributed to their low loading efficiency of miRNA. These findings suggest that LPEx may be more advantageous than LP or wEV for delivering miRNA. Moreover, the lysosomal escape capabilities of miRNA delivered via LP, LPEx, and wEV were compared. The findings revealed that miRNA encapsulated by LP exhibited a low rate of lysosomal escape following cellular uptake (Fig. 7A, B) [50, 51]. In contrast, miRNA delivered

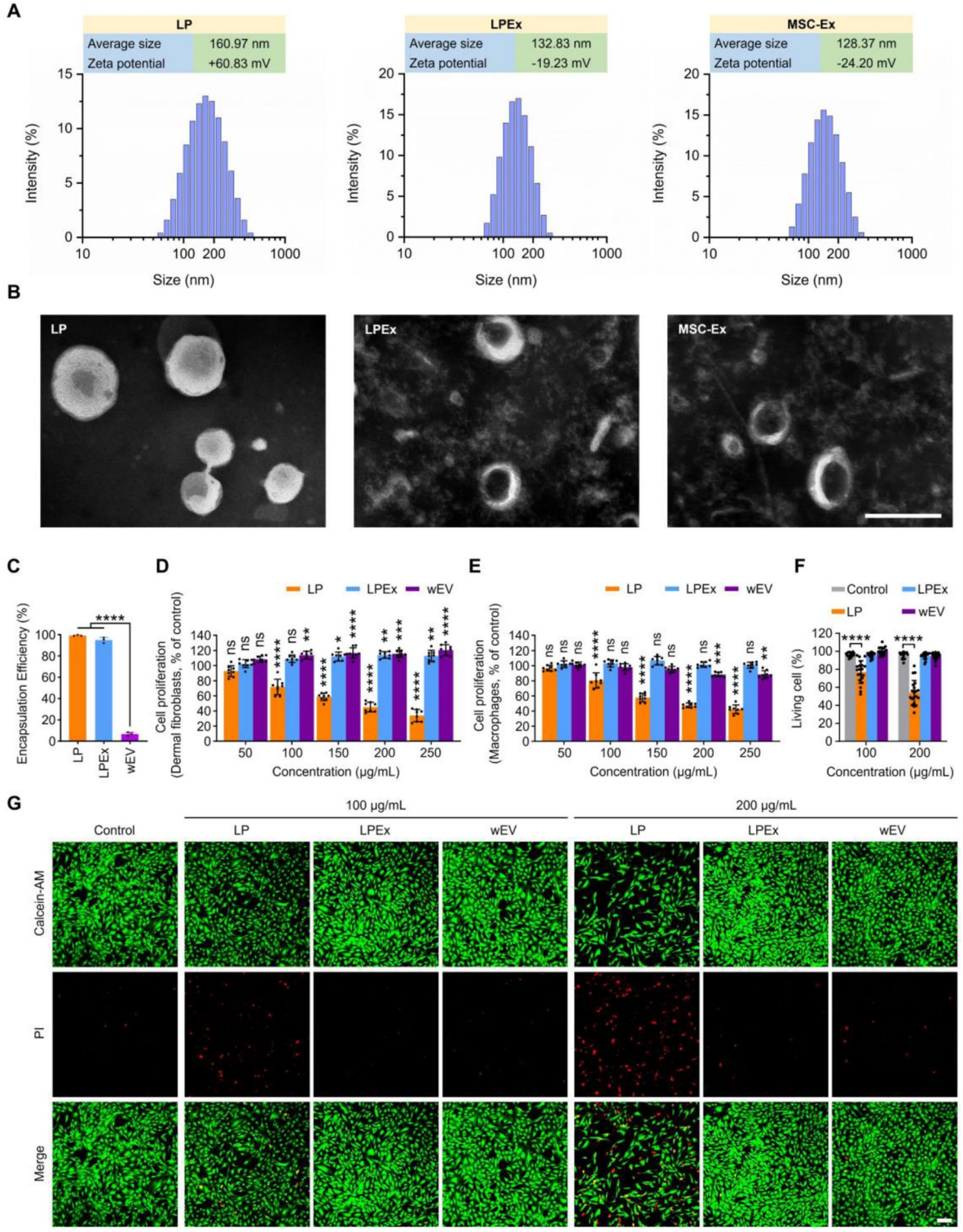

Fig. 6 Characterization and cytotoxicity assessment of LPEx. (**A**) Hydrated particle sizes and zeta potential of the obtained nanovesicles. (**B**) Representative images of TEM analysis of the nanovesicles. Scale bar: 100 nm. (**C**) Comparison of LP, LPEx, and wEV encapsulation efficiency for miRNA. (**D**, **E**) The CCK-8 assay performed on dermal fibroblasts (**D**) and macrophages (**E**), respectively. (**F**, **G**) Quantitative analysis (**F**) and representative images (**G**) of live/dead staining on dermal fibroblasts. Live cells were labeled by Calcein-AM (green), and dead cells were labeled by PI (red). Scale bar: 100 μm. All statistical analyses were performed using one-way ANOVA with Tukey's multiple comparison test. Specifically, for (**D**) and (**E**), significance was compared with the control group. $^{*}P < 0.05$, $^{**}P < 0.01$, $^{***}P < 0.001$, $^{****}P < 0.0001$, ns, not significant. All data are presented as mean ± S.D

by LPEx and wEV demonstrated significantly higher rates of lysosomal escape than miRNA delivered via LP upon entering the cells. Furthermore, we investigated the lysosomal escape kinetics of miRNA delivered by LPEx. It was found that in dermal fibroblasts, the lysosomal escape rate of miRNA was relatively low at 6 h post-cellular uptake, but it increased rapidly and reached its peak at 12 h (Figure S17). In macrophages, the lysosomal escape rate of miRNA delivered by LPEx was slower, reaching its maximum at 24 h post-cellular uptake.

In order to elucidate the mechanism of cellular uptake of LPEx and why LPEx exhibit high lysosomal escape properties, specific receptor-mediated clathrin-dependent internalization, micropinocytosis, energy-dependent endocytosis, and caveolin-dependent internalization were blocked by using chlorpromazine (CPZ), amiloride, NaN_3, and nystatin, respectively [52]. We found that CPZ and nystatin significantly inhibited cellular uptake of LPEx, whereas amiloride and NaN_3 had no significant effect on LPEx entry (Fig. 7C, D). It suggests that cells mainly rely on specific receptor-mediated clathrin-dependent internalization and caveolin-dependent internalization for the uptake of LPEx. Both types of internalization depend on the interaction between ligands on the surface of the vesicles and receptors on the cell surface. Previous studies have shown that the key reason mammalian exosomes have a high ability to escape from lysosomes is due to the interaction between exosomal surface ligands and cell surface receptors [53]. Plant-derived extracellular vesicles share similar structures and compositions with animal-derived exosomes [37, 38], which may account for their high lysosomal escape rates. However, due to the current limited research on plant extracellular vesicles, it is not yet clear which receptors on the surface of wEV are responsible. LPEx were obtained by the fusion of LP and wEV, and their surface has ligands derived from wEV. These ligands enable LPEx to have endocytic pathways similar to exosomes, which may be the reason for their high lysosomal escape ability.

Subsequently, to evaluate whether LPEx-delivered miRNAs can fully manifest their biological functions, LPEx, LP, and wEV were loaded with the screened 28 miRNAs to obtain LPEx-R, LP-R, and wEV-R, respectively. The percentage content of each miRNA among these 28 miRNAs is equivalent to their natural proportion in $EX_{1.25}$ (Table S4). The pro-proliferative, anti-inflammatory, and anti-fibrotic efficacies of LPEx-R, LP-R, and wEV-R were then comparatively assessed against those of $EX_{1.25}$ and miR-NC-loaded LPEx (LPExNC). The results indicated that both $EX_{1.25}$ and LPEx-R markedly enhanced dermal fibroblast proliferation (Fig. 7E, F). In contrast, LP-R and LPExNC did not significantly influence cell proliferation. In anti-inflammatory assays, all nanovesicle groups, with the exception of LPExNC, exhibited significant anti-inflammatory effects (Fig. 7G, H and Figure S18). Notably, LPEx-R surpassed $EX_{1.25}$ in efficacy, demonstrating the most potent anti-inflammatory activity (0.40-fold of NO expression vs. $EX_{1.25}$ group). Anti-fibrotic experiments revealed that $EX_{1.25}$ and LPEx-R both significantly reduced fibrogenesis, exhibiting comparable inhibitory effects (Fig. 7I-K). The remaining three groups of vesicles showed either no effect or only a mild inhibitory effect on fibrogenesis. These results indicate that miRNAs delivered via LPEx can efficiently enter cells and fully exert their regulatory functions on cellular behavior.

LPEx-R significantly enhance burn wound healing and reduce scar formation

Prior to assessing the in vivo efficacy of LPEx in promoting wound healing and preventing scarring, their biocompatibility was evaluated. The subcutaneous tissues of mice injected with LP, LPEx, and wEV showed no apparent necrosis and no expression of IL-1β and TNF-α. In contrast, the subcutaneous tissue of mice injected with egg white exhibited significant necrotic areas (Figure S19A) and expressed high levels of IL-1β and TNF-α (Figure S19B). In another test, hematological examinations of mice receiving LP, LPEx, and wEV treatment (intravenous injection) showed normal values for each indicator. However, mice injected with LPS exhibited abnormal ratios of lymphocytes, monocytes, and eosinophils, as well as abnormal lymphocyte and platelet counts in the blood (Table S5). Additionally, no significant upregulation in the expression levels of IL-1β and TNF-α was observed in the serum of mice injected with LP, LPEx, or wEV (Figure S20).

To investigate the organ distribution of LP, LPEx, and wEV after entering the body, these nanovesicles were intravenously injected into mice, respectively. It was found that 48 h later, LPEx and wEV were distributed in the brain, lungs, liver, spleen, and kidneys of the mice, but were mainly concentrated in the liver and kidneys (Figure S21). In contrast, LP were only detected in the liver and kidneys. Moreover, the total fluorescence intensity of LP was significantly lower than that of the LPEx and wEV groups. This may be attributed to the adsorption of LP with proteins in the blood, forming larger particles (as shown in Figure S13), which are subsequently cleared by immune cells. These results indicate that LPEx and wEV are more stable in vivo and more capable of withstanding long-circulation compared to LP. Given that LP, LPEx, and wEV are primarily distributed in the liver and kidneys, their potential impact on hepatic and renal function was evaluated. The mice received intravenous injection of normal saline (control), LP, LPEx, and wEV showed normal serum alanine aminotransferase (ALT), aspartate aminotransferase (AST), blood urea nitrogen (BUN),

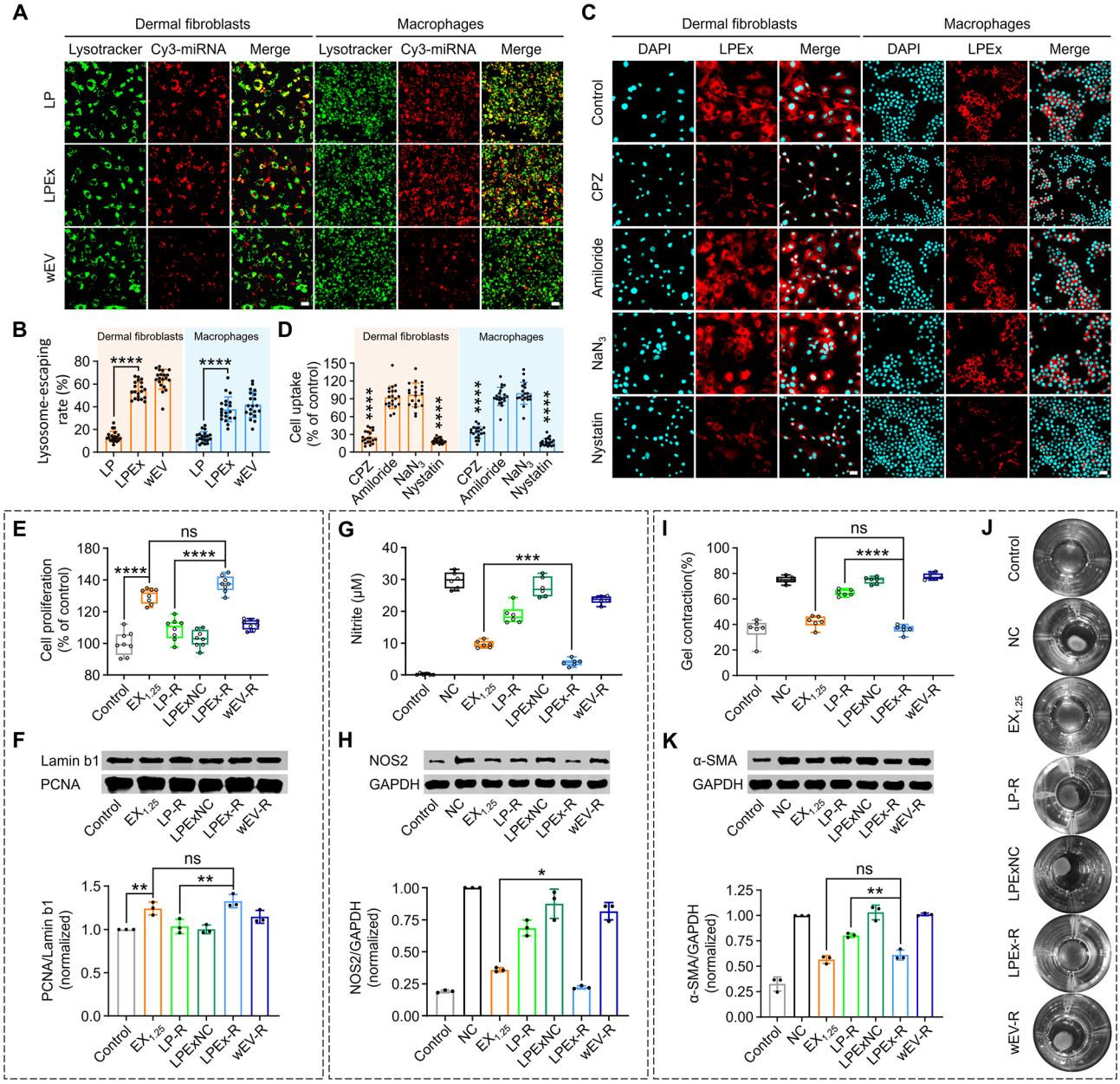

Fig. 7 Cellular uptake and miRNA delivery efficiency of LPEx. (**A**) Representative images of the co-localization of lysosomes (green) with Cy3-miRNA (red). Scale bar: 20 μm. (**B**) Quantitative analysis of lysosomal escape efficiency. (**C**) Representative images of the cellular uptake of LPEx on dermal fibroblasts and macrophages receiving various inhibitor treatments. Nuclei were labeled with DAPI (blue), and LPEx was labeled red. Scale bar: 20 μm. (**D**) Quantitative analysis of the mean cellular uptake of LPEx in each group. (**E**, **F**) Effects of the 28 miRNAs encapsulated in different nanocarriers on dermal fibroblast proliferation. (**G**, **H**) Effects of the 28 miRNAs encapsulated in different nanocarriers on LPS-induced inflammatory responses. (**I-K**) Anti-fibrotic effect of the 28 miRNAs encapsulated in different nanocarriers on TGF-β1-activated dermal fibroblasts. All statistical analyses were performed using one-way ANOVA with Tukey's multiple comparison test. Specifically, for (**D**), significance was compared with the control group. *$P < 0.05$, **$P < 0.01$, ***$P < 0.001$, ****$P < 0.0001$, ns, not significant. All data are presented as mean ± S.D

and creatinine (CR) levels (Figure S22A, B). However, in mice treated with carbon tetrachloride (CCl4), there was a significant elevation in the levels of serum ALT and AST. Likewise, mice subjected to cisplatin (DDP) treatment exhibited a notable increase in BUN and CR levels in their serum, while other groups did not show such an increase. The result of H&E staining further confirms that LP, LPEx, and wEV are harmless to the liver and kidneys. Conversely, CCl4 and DDP caused significant damage to the liver (necrosis and ballooning degeneration.) and kidney (tubular degeneration, necrosis, and inflammatory cell infiltration), respectively (Figure S22C, D).

Finally, the impact of LPEx-R on deep second-degree burn wound healing and scar formation was evaluated

(Fig. 8A) and compared with that of $EX_{1.25}$ and the HiPerFect-R (the HiPerFect transfection reagent loaded with the 28 miRNAs). The results demonstrated that, compared to the control group, both $EX_{1.25}$ and LPEx-R significantly promoted wound repair and reduced scar formation (Fig. 8B, C), while HiPerFect-R showed only a slight advantage over the control. Meanwhile, the wound healing rate in the $EX_{1.25}$ group and the LPEx-R group showed no significant difference.

Next, the microscopic structure of the wounds in each group was examined by H&E staining and Masson's staining. The results of H&E staining (Fig. 8D) indicated that by Day 6, the control group exhibited minimal formation of granulation tissue, whereas the wounds in other groups had already developed some granulation tissue. Subsequently, on Day 10 and Day 14, the wounds in the $EX_{1.25}$ and LPEx-R groups exhibited accelerated extracellular matrix synthesis as compared with the control and HiPerFect-R groups. By Day 18, the LPEx-R group displayed enhanced extracellular matrix remodeling and regeneration of skin appendages (marked with blue arrows) as compared to the $EX_{1.25}$ group. In contrast, the wound tissues in the control group and the HiPerFect-R group exhibited poor remodeling of the extracellular matrix.

Collagen plays a crucial role in wound repair. It provides structural support and a scaffold for cell attachment in the wound tissue, promotes cell migration, proliferation, and differentiation, and regulates inflammatory responses and granulation tissue formation [54]. As shown in Fig. 9A and B, both LPEx-R and $EX_{1.25}$ significantly promoted collagen synthesis in the wound healing process, outperforming the control and HiPerFect-R. On Day 14, the LPEx-R group exhibited the most densely and orderly arranged collagen fibers in the wound area, indicating the highest degree of remodeling. This was followed by the $EX_{1.25}$ group. Although the HiPerFect-R group demonstrated a higher amount of collagen compared to the control group, the collagen was predominantly distributed in a parallel manner, which is characteristic of scar tissue [55], suggesting insufficient collagen remodeling in this group. As for the control group, the collagen content remained relatively low even by Day 14, indicating a slower rate of wound healing.

The content of PCNA can reflect the proliferative activity of cells in wound tissue. A high level of PCNA indicates that the wound is in an active repair phase, with vigorous cell division and proliferation, which promotes tissue regeneration and repair [56]. During the wound healing process, the expression level of PCNA undergoes dynamic changes. In the early and middle stages, the content of PCNA gradually increases to facilitate rapid wound filling and tissue regeneration. In the later stage, the expression of PCNA gradually decreases as the wound enters the remodeling phase, where excess cells are eliminated through apoptosis or macrophage phagocytosis, promoting wound maturation and tissue remodeling [57]. On day 6, the PCNA content

in the wound tissues of the $EX_{1.25}$ and LPEx-R groups was significantly higher than that in the control group (Fig. 9C, D). Although the PCNA content in the HiPerFect-R group was higher than that in the control group, it was lower than that in the $EX_{1.25}$ and LPEx-R groups. These results indicate that on day 6, the wounds in the $EX_{1.25}$ and LPEx-R groups were in a highly active repair phase. By day 10, the PCNA content in the wound tissues of the $EX_{1.25}$ and LPEx-R groups had markedly decreased, suggesting that the cells in these wounds had exited the rapid proliferation phase and were gradually transitioning into the remodeling stage. In contrast, the PCNA content in the control group remained relatively high, indicating that the wounds in this group were still in the proliferation phase. These results further consolidated the conclusions drawn from Fig. 8B and C, demonstrating that $EX_{1.25}$ and LPEx-R indeed significantly promoted wound healing.

Inflammatory responses have a direct impact on wound healing and scar formation. An appropriate inflammatory response aids in wound healing, while excessive or abnormal inflammatory responses can lead to scar formation and delayed healing. As one of the most difficult wound types to treat, burn wounds often accompany severe and persistent inflammatory responses. Therefore, modulating the inflammatory response is an important therapeutic strategy for improving burn wound healing and reducing scar formation [58]. Immunofluorescence staining for IL-1β and TNF-α was performed on the wound tissues of all groups (Figure S23), revealing that the wounds in the $EX_{1.25}$ and LPEx-R groups by day 6 and day 10 exhibited significantly lower expression levels of IL-1β and TNF-α in comparison to the control group. On Day 10, the HiPerFect-R group also exhibited significantly lower levels of inflammatory cytokines in the wounds compared to the control group, yet higher than those in the wounds of the $EX_{1.25}$ and LPEx-R groups. These results indicate that both $EX_{1.25}$ and LPEx-R exhibited good anti-inflammatory effects in wound healing, while the in vivo anti-inflammatory effect of HiPerFect-R was inferior to that of $EX_{1.25}$ and LPEx-R.

α-SMA is a marker of scarring. To further ascertain the anti-scar formation effects of HiPerFect-R, $EX_{1.25}$, and LPEx-R, we conducted α-SMA immunofluorescence staining on the wound tissues. The results (Fig. 9E, F) displayed that on Day 14 and Day 18, the wounds in the $EX_{1.25}$ and LPEx-R groups exhibited considerably lower expression levels of α-SMA in comparison to the control group. On Day 18, the expression of α-SMA in the wounds of the HiPerFect-R group was also lower than

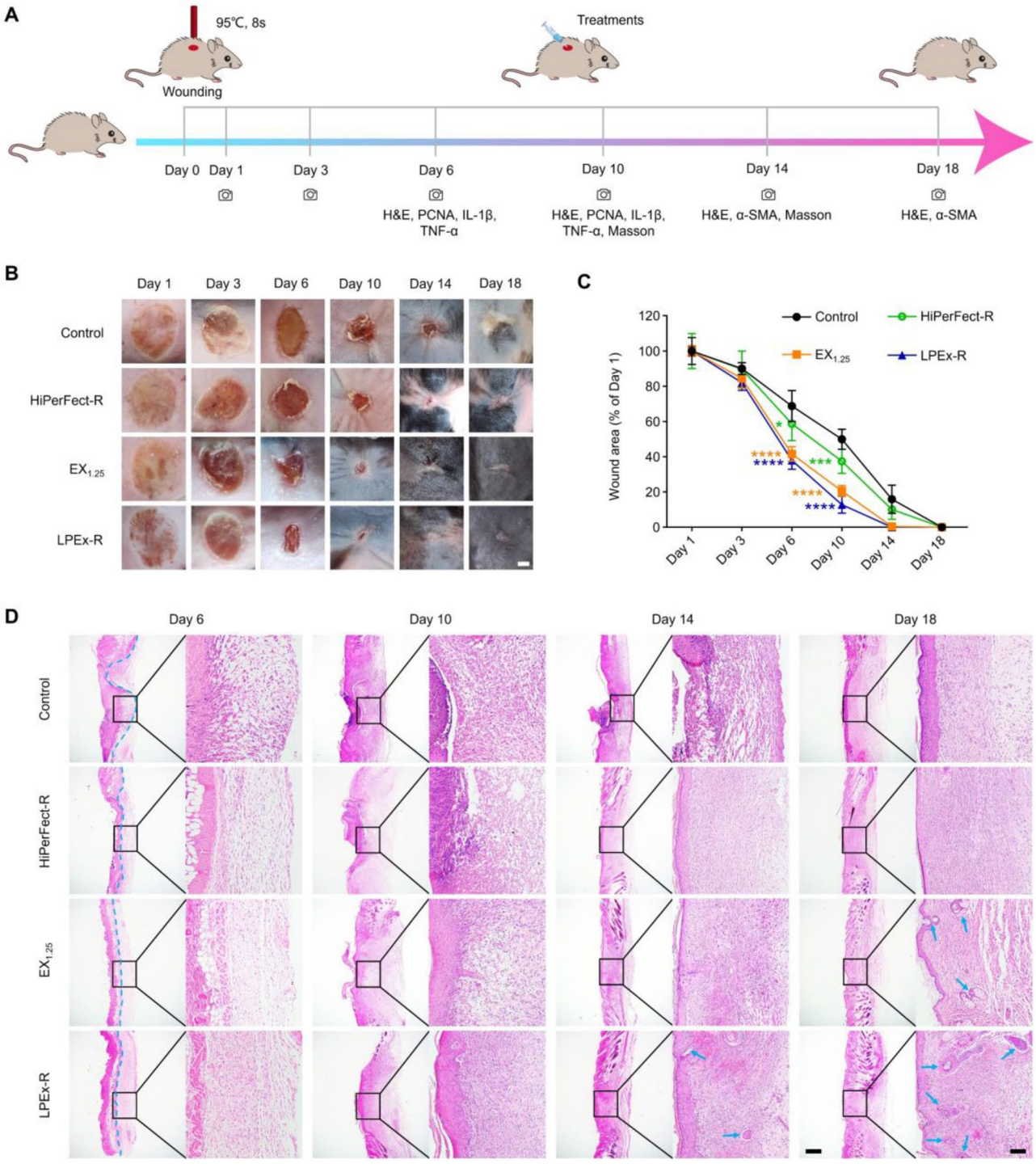

Fig. 8 Comparative study of the pro-healing and scar-preventive properties of $EX_{1.25}$ and LPEx-R on burn wounds. (**A**) Schematic diagram of the in vivo burn wound healing experiment. (**B**) Photographs of representative wounds from each group on different post-wound days. Scale bar: 2 mm. (**C**) Quantification of the residual wounds; significance was compared with the control group. (**D**) H&E staining of wound tissues. In the images of the wound tissue on Day 6, the necrotic tissue is on the left side of the blue dashed line, while the regenerated tissue is on the right side of the blue dashed line. Scale bar: 200 μm–50 μm. Statistical analysis was performed by one-way ANOVA with Tukey's multiple comparison test, $^{*}P < 0.05$, $^{***}P < 0.001$, $^{****}P < 0.0001$. Data are presented as mean ± S.D

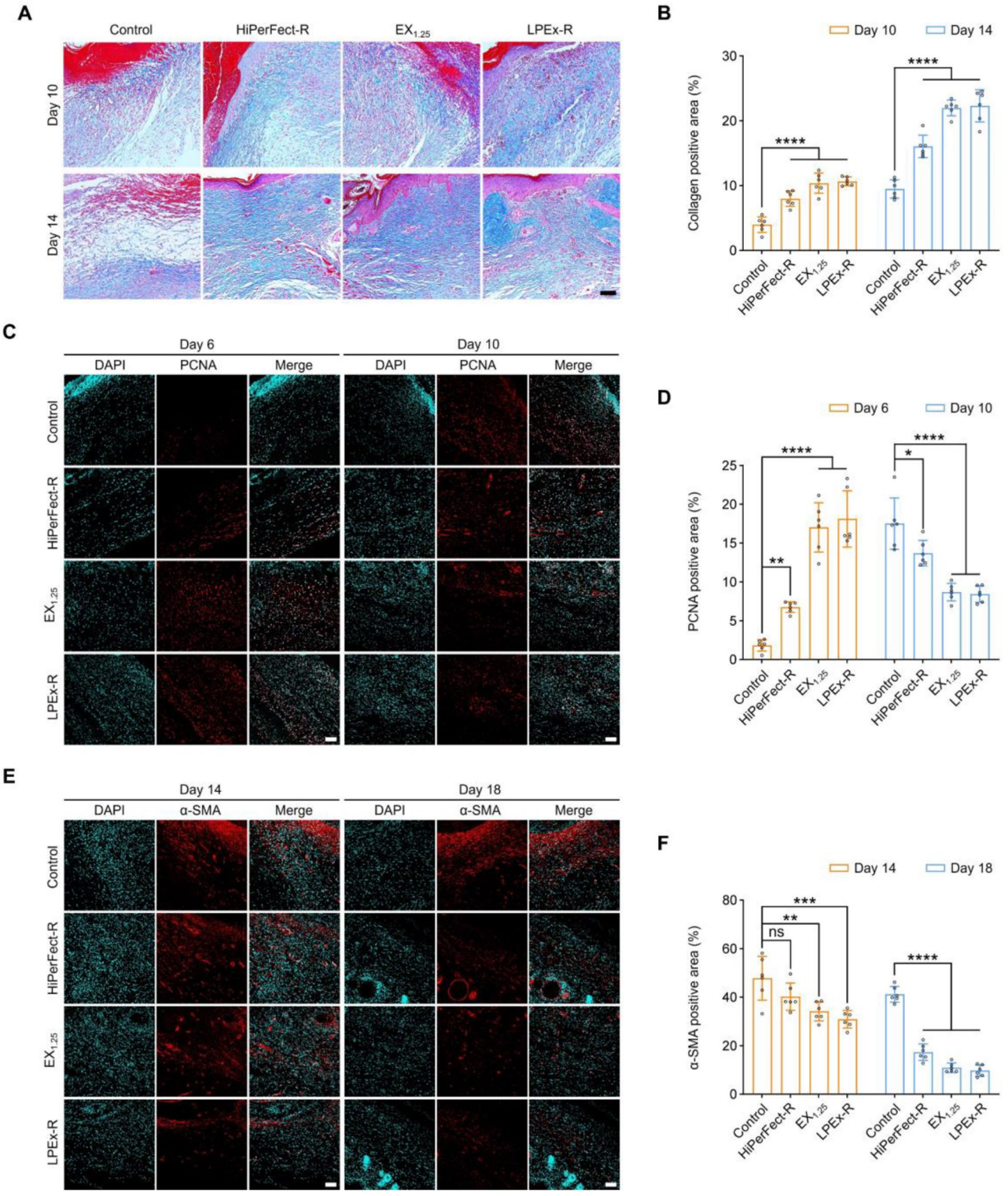

Fig. 9 Masson's staining and immunofluorescence staining for PCNA and α-SMA in wound tissue. (**A**, **B**) Representative images and quantitative analysis of Masson's staining of wound tissues. Scale bar: 50 μm. (**C**, **D**) Representative images and quantitative analysis of immunofluorescence staining of PCNA (red) of wound tissues. Scale bar: 50 μm. (**E**, **F**) Representative images and quantitative analysis of immunofluorescence staining of α-SMA (red) of wound tissues. Scale bar: 50 μm. All statistical analysis was performed by one-way ANOVA with Tukey's multiple comparison test, $^{*}P < 0.05$, $^{**}P < 0.01$, $^{***}P < 0.001$, $^{****}P < 0.0001$, ns, not significant. All data are presented as mean ± S.D

that in the control group. These results demonstrated that HiPerFect-R, $EX_{1.25}$, and LPEx-R indeed suppressed scar formation.

The in vivo wound healing results indicate that LPEx can effectively deliver the screened 28 miRNAs to wound tissue and exerts strong pro-regenerative, anti-inflammatory, and anti-fibrotic effects, providing favorable conditions for the rapid repair of wounds and the prevention of scars. The wounds treated with LPEx-R showed similar or better outcomes compared to $EX_{1.25}$ in terms of healing rate, collagen remodeling, and regeneration of skin appendages. These results provided a solid foundation for the further clinical application of LPEx-R.

One of the major concerns in the clinical translation of LPEx-R is achieving scalable production while ensuring consistent quality. In this study, the preparation processes of both LP and wEV are not complex and allow for swift large-scale production. Moreover, the fusion of LP-miR with wEV to obtain LPEx-R is a well-established process, ensuring the rapid and stable production of LPEx-R. Another concern in clinical application is the cost. LPEx-R effectively addresses this challenge by virtue of its cost-effectiveness. Watermelon is a widely available and inexpensive agricultural product, and its extracellular vesicles can be isolated using straightforward and scalable methods. Furthermore, the synthesis of LP is a robust and cost-effective process. By combining these two components, the overall production cost of LPEx-R is substantially lower than that of natural MSC-Ex. In our laboratory, the cost of preparing an equivalent quantity of LPEx-R is approximately 1/120 that of preparing MSC-Ex. This cost advantage of LPEx-R makes them more accessible for widespread clinical use.

Even though LPEx-R exhibits greater potential for widespread clinical application compared to natural MSC-Ex, there are still some unresolved issues that need to be addressed. For example, plant extracellular vesicles contain a variety of nucleic acids, such as miRNAs, which can exert a cross-kingdom effect in animal cells, regulating specific cellular functions across species [59]. However, it remains unclear whether the regulatory effects of nucleic acid components in wEV are beneficial or harmful to the organism in the context of long-term exposure. Further research is still needed to explore this question. In addition, the isolation and purification of plant extracellular vesicles still face some challenges, and a unified "gold standard" has not yet been established [60]. In the future, it will be necessary to conduct in-depth research into the biological characteristics of wEV in order to develop more efficient and specific isolation and purification methods, ensuring their safety and efficacy. Meanwhile, standardized production and quality control systems need to be established to guarantee the reliability and reproducibility of LPEx-R in clinical applications. Finally, neither wEV nor LPEx have antibacterial properties (Figure S24). However, wounds are often prone to bacterial infections due to improper or untimely treatment. Since exosomes or exosome-like vesicles are often required to be loaded into hydrogels for clinical use, we may need to develop an LPEx-R-hydrogel system in the future, endowing the hydrogel with antibacterial capabilities while achieving the stable release of LPEx-R.

Conclusions

In the present study, we have identified 28 miRNAs within MSC-Ex that play key roles in facilitating wound healing and preventing scar formation. Subsequently, we fabricated novel exosome-like vesicles that mimic the intrinsic properties of natural MSC-Ex to deliver these miRNAs, thereby endowing them with therapeutic efficacy comparable to the native MSC-Ex for the repair of deep second-degree burn wounds. Collectively, this research introduces a method for the stable and large-scale production of exosome-like vesicles, overcoming the challenge of mass production associated with MSC-Ex. Future studies should focus on optimizing the production process and evaluating long-term safety. With further development, the LPEx-R developed in this study have the potential to revolutionize regenerative medicine and make exosome-based therapies more accessible to patients worldwide.

Materials and methods

Education of MSCs and preparation of MSC-Ex

Macrophages (RAW264.7, ATCC) were seeded (4×10^4 cells/cm^2) and cultured with Dulbecco's modified Eagle's medium (DMEM) containing 10% fetal bovine serum, 100 U/mL penicillin, and 100 μg/mL streptomycin. Twenty-four hours later, the cells were activated with LPS (1 μg/mL) for 12 h. Subsequently, the culture medium was replaced with fresh medium (free of LPS), and the cells were further incubated for 12 h. Meanwhile, a control group of macrophages without LPS treatment was also prepared. Following this, both groups of cells and cell-conditioned media were collected. The levels of NO, IL-1β, and TNF-α in the cell-conditioned media were quantified using the Griess reagent (Beyotime, China) for NO detection ($n = 6$), and enzyme-linked immunosorbent assay kits (Fusheng, China) for the measurement of IL-1β and TNF-α ($n = 6$). Additionally, the expression of NOS2 within the cells was ascertained through western blotting analysis. After that, the conditioned medium collected from the LPS-activated macrophages was loaded into a dialysis bag with a molecular weight cutoff of 3500 Da. The bag was then submerged in polyethylene glycol (PEG) powder (average molecular weight of 20,000 Da) for concentration. This process yielded a concentrated conditioned medium (CCM), which was reduced to a

final volume of 10% of its original volume. Subsequently, CCM was aseptically filtered through a 0.22 μm membrane and then incorporated into the complete culture medium for murine bone marrow-derived mesenchymal stem cells (Cyagen, China) at concentrations of 10% (v/v), 5% (v/v), 2.5% (v/v), and 1.25% (v/v), yielding induction media designated as IM_{10}, IM_5, $IM_{2.5}$, and $IM_{1.25}$, respectively.

IM_{10}, IM_5, $IM_{2.5}$, and $IM_{1.25}$ were used to induce MSCs for a 48-hour period. A control group of MSCs was maintained and cultured for 48 h using medium without CCM. The cells cultured by IM_{10}, IM_5, $IM_{2.5}$, $IM_{1.25}$, and medium without CCM were termed MSC_{10}, MSC_5, $MSC_{2.5}$, $MSC_{1.25}$, and MSC_0, respectively. Then, the cells were digested with trypsin and passaged in a complete culture medium containing 4% exosome-free fetal bovine serum (VivaCell, China), followed by a 72-hour incubation. After this, both the cells and the culture supernatants were collected. Exosomes were isolated by ultracentrifugation [60] from the collected supernatants and characterized using nanoparticle tracking analysis, transmission electron microscopy, and western blotting analysis for the expression of CD9, CD81, and GAPDH.

In vitro functional assessment of MSC-Ex

Exosomes secreted from MSC_0, MSC_{10}, MSC_5, $MSC_{2.5}$, and $MSC_{1.25}$ were designated as EX_0, EX_{10}, EX_5, $EX_{2.5}$, and $EX_{1.25}$, respectively. Throughout the investigation of exosome functionality, dermal fibroblasts and macrophages were treated with different groups of MSC-Ex at 20 μg/mL and 40 μg/mL (protein concentration), respectively. The cells of the control group and the NC group were treated with culture medium devoid of exosomes.

For the cell proliferation experiment, dermal fibroblasts were seeded (1×10^4 cells/cm^2) and cultured with DMEM containing 10% fetal bovine serum, 100 U/mL penicillin, and 100 μg/mL streptomycin. Twenty-four hours later, cells were treated with various groups of MSC-Ex. After a 12-hour incubation, the culture medium was removed and replaced with fresh culture medium without MSC-Ex for an additional 36-hour incubation period. Subsequently, cell proliferation was assessed using the CCK-8 assay (Solarbio, China) and western blotting analysis to detect PCNA expression levels. For the CCK-8 assay, cell proliferation capacity was calculated using the following formula:

$$\text{Cell proliferation}\,(\%) = \frac{OD_t - OD_b}{OD_{ctl} - OD_b} \times 100 \quad (1)$$

where OD_t, OD_b, and OD_{ctl} represent the OD450 values of the tested group ($n = 8$), the blank control, and the control groups, respectively.

For the evaluation of anti-inflammatory capacity, macrophages were pre-seeded with a density of 4×10^4 cells/cm^2. Twenty-four hours later, the cells were treated with various groups of MSC-Ex for 12 h. Then, the culture medium of all experimental and NC groups was replaced with fresh medium containing 1 μg/mL of LPS. The control group was treated with fresh medium without LPS. The cells were incubated for an additional 12 h. Subsequently, the content of NO, IL-1β, and TNF-α in the medium was measured ($n = 6$), and the relative expression of NOS2 in macrophages was also assessed through western blotting analysis.

For the evaluation of anti-fibrotic capability, dermal fibroblasts were treated with various groups of MSC-Ex for 24 h. Afterward, the culture medium of all experimental and NC groups was replaced with fresh medium containing 20 ng/mL of TGF-β1 (Pricella, China). The control group was treated with fresh medium without TGF-β1. The cells were incubated for an additional 48 h. Subsequently, a portion of the cells were subjected to a gel contraction assay. Another portion of the cells underwent western blotting analysis to determine the relative levels of α-SMA. For the gel contraction assay, the specific experimental steps are as follows:

First, mouse tail type I collagen was prepared using the method described by Rittié [61]. The collagen solution (5 mg/mL) was then diluted with DMEM (containing 10% fetal bovine serum, 100 U/mL penicillin, and 100 μg/mL streptomycin), and fibroblasts were added and suspended evenly. The final concentrations of collagen and cells were 1 mg/mL and 2×10^5 cells/mL, respectively. The solution was added to a 48-well culture plate (300 μL per well) and incubated at 37 °C for 24 h ($n = 6$). Subsequently, the digital images of the contracting lattices were taken, with the collagen matrix areas calculated using the ImageJ software. The gel contraction rate was calculated using the following formula:

$$\text{Gel contraction}\,(\%) = \frac{A_0 - A_t}{A_0} \times 100 \quad (2)$$

where A_0 and A_t indicate the area of the collagen matrix before and after the contraction, respectively.

In vivo functional assessment of MSC-Ex on burn wounds

C57BL/6 mice were used in this experiment; the hair on the dorsal part was shaved, and a 7-mm-diameter aluminum rod with a temperature of 95 ℃ was placed on the skin for 8 s to induce deep second-degree burn wounds (day 0). For each group, eight animals were randomly assigned. On days 0, 3, 6, and 10, a total volume of 20.0 μL of sterile PBS solution (control) and 1.0 μg/μL (protein concentration) of EX_0 or $EX_{1.25}$ were subcutaneously injected around the wound of each mouse in each group

at multi-point injection, respectively. The appearance of the wounds was photographed on days 1, 3, 6, 10, 14, and 18. The wound areas were measured by the ImageJ software, and the wound closure rate was calculated using the following formula:

$$\text{Wound closure } (\%) = \frac{A_1 - A_t}{A_1} \times 100 \quad (3)$$

where A_1 represents the areas of wounds at day 1, and A_t represents the areas of wounds at the 3rd, 6th, 10th, 14th, and 18th days.

In addition, at the 6th, 10th, 14th, and 18th days, one mouse from each group was randomly sacrificed, and the skins, including the whole wound and the adjacent healthy tissue, were excised, immersed in a 4% formaldehyde solution, dehydrated, embedded, and cut into 5 μm-thick slices. After this, the slices were used for further histological analysis.

miRNA sequencing

Total RNA was extracted from EX_0 and $EX_{1.25}$ using TRIzol® Reagent (Invitrogen, USA). The ligation of activated 5' and 3' adaptors, as well as the first-strand cDNA transcription, was performed following the instructions of the TruSeq™ Small RNA Sample Prep Kit (Illumina, CA), respectively. Subsequently, a 12-cycle PCR reaction was carried out, and fragments of the appropriate size were isolated using a 6% Novex TBE PAGE gel. After quantification using the TBS380 system, a single-end RNA-seq sequencing library was generated and sequenced using the Illumina NovaSeq 6000 sequencer. Raw data were processed using fastp [62] and the fastx toolkit software. Known miRNAs were identified from the miRBase 22.0 database [63], and novel miRNAs were predicted using the miRDeep2 software [64]. The expression level of each miRNA was calculated according to the transcripts per million reads (TPM) method. In silico analysis of target gene predictions for miRNAs was performed using miRanda, TargetScan, and RNAhybrid [65–67].

Functional assessment of the pre-screened 32 miRNAs

HiPerFect transfection reagent (Qiagen, Germany) was employed for miRNA transfection. For dermal fibroblasts and macrophages, the transfection concentrations of the 32 miRNA mimics was 50 nM and 100 nM, respectively. The control and NC group cells were transfected with miRNA mimic negative control (miR-NC) at the same concentration as the corresponding experimental groups. The cell proliferation assays, anti-inflammatory assays, and anti-fibrotic assays were performed following the methods described above.

Isolation of extracellular vesicles from watermelon

The fresh watermelon (*Citrullus lanatus*) was peeled, and the flesh was subsequently cut into small pieces. These pieces were then placed into a non-woven fabric bag and subjected to pressure to extract the juice. The juice was filtered through a non-woven gauze and then successively centrifuged at 500 ×g (10 min), 4000 ×g (20 min), and 12,000 ×g (30 min) to remove cellular debris and other large particles. Subsequently, 40% (w/v) PEG 6000 was added to the watermelon juice to achieve a final concentration of 8% (w/v). The mixture was left to stand at 4 °C overnight, followed by centrifugation at 12,000 ×g (20 min) the next day. The pellet was dissolved in a small amount of PBS (0.01 M, pH 7.4) and subjected to an additional 12,000 ×g centrifugation (10 min) to remove insoluble matter. The supernatant was wEV, and the protein concentration of wEV in the supernatant was measured.

Metabolomics analysis of wEV

After freeze-drying the prepared wEV, they were dissolved in 70% methanol, filtered through a 0.22 μm membrane. The subsequent metabolomics analysis was conducted using an ultra-performance liquid chromatography system (ExionLC™ AD, https://sciex.com.cn/) coupled with a tandem mass spectrometry system (https://sciex.com.cn/). The experimental conditions were as follows: The column used was an Agilent SB-C18 (1.8 μm, 2.1 mm × 100 mm). The mobile phase consisted of solvent A (pure water with 0.1% formic acid) and solvent B (acetonitrile with 0.1% formic acid). The elution conditions were as follows: at 0.00 min, the proportion of solvent B was 5%; within 9.00 min, the proportion of solvent B was linearly increased to 95% and maintained at 95% for 1 min; from 10.00 to 11.10 min, the proportion of solvent B was reduced to 5% and equilibrated at 5% until 14 min. The flow rate was set at 0.35 mL/min, the column temperature was maintained at 40 °C, and the injection volume was 2 μL. The effluent was alternately directed to an ESI-triple quadrupole-linear ion trap (QTRAP)-MS. Compound identification was carried out based on the secondary mass spectrometry (MS/MS) information, while compound quantification was accomplished using the multiple reaction monitoring mode of the triple quadrupole mass spectrometry.

Preparation of LPEx

A total mass of 60 μg of cationic LP was mixed with 0.1 nmol of miRNA mimics to form LP-miR. Subsequently, the LP-miR solution was mixed with 100 μg (mass of protein) of wEV to obtain the LP-miR-wEV complex, and the complex was allowed to stand at room temperature for 30 min. Successively, the LP-miR-wEV complex was sequentially extruded through polycarbonate membranes with pore sizes of 800 nm, 400 nm, 200 nm, and

100 nm to obtain LPEx. The hydrated particle sizes and zeta potential of LP, wEV, and LPEx are measured using a Zetasizer (Nano-ZS 90, Malvern, UK), and these values are compared with those of MSC-Ex.

Encapsulation efficiency

Four RNase-free centrifuge tubes were labeled as I, II, III, and IV. In tube I, 0.5 nmol of Cy3-miRNA mimic negative control (Cy3-miR-NC) was added, and the volume was adjusted with pure water to 0.5 mL. In tube II, 0.5 nmol of Cy3-miR-NC was mixed with 300 μg of LP to prepare the LP-Cy3-miR-NC complex (0.5 mL). In tube III, 0.5 mL of LPEx encapsulated with 0.5 nmol of Cy3-miR-NC were prepared as described above. In tube IV, 500 μg (mass of protein) of wEV and 0.5 nmol of Cy3-miR-NC were added (0.5 mL), and electroporation was processed as previously described [68]. Subsequently, the solutions in tubes II, III, and IV were centrifuged at 200,000 ×g for 60 min, the supernatants were discarded, and the pellet of each tube was dissolved in 0.5 mL of pure water. The absorbance values of the solutions in each tube at 550 nm were measured, denoted as A_I, A_{II}, A_{III}, and A_{IV}, respectively. The encapsulation efficiency was calculated using the following formula:

$$\text{Encapsulation Efficiency}\ (\%) = \frac{\text{Ax}}{\text{A}_\text{I}} \times 100 \quad (4)$$

where A_x represents A_{II}, A_{III}, or A_{IV}.

Cellular uptake kinetics of LP, LPEx, and wEV

To evaluate the cellular uptake kinetics of LP, LPEx, and wEV, dermal fibroblasts and RAW264.7 cells were initially seeded in confocal microscopy dishes. Once the cells reached approximately 70% confluence, the original culture medium was removed and replaced with transfection medium containing LP, LPEx, or wEV loaded with Cy3-miR-NC at a concentration of 100 nM. After incubation for 6, 12, or 24 h, the cells were taken out, and their nuclei were stained with DAPI. The uptake of these nanovesicles by the cells was then visualized using confocal microscopy.

Cytotoxicity

The CCK-8 assay and the live/dead cell fluorescence staining were carried out in this portion of the experiments. Typically, every 20 μg of LP was mixed with 0.1 nmol of miR-NC, LPEx were prepared as aforementioned. Subsequently, corresponding transfection culture media were formulated to achieve concentrations of LP, LPEx, or wEV at 50 μg/mL, 100 μg/mL, 150 μg/mL, 200 μg/mL, and 250 μg/mL. These transfection-working solutions were used to culture dermal fibroblasts and macrophages that were pre-seeded in a 96-well plate ($n = 8$), and control groups containing only basic culture medium were established. After 24 h, the cell viability of each group was assessed using the CCK-8 assay. As for the live/dead cell fluorescence staining, dermal fibroblasts and macrophages were pre-seeded on confocal-specific dishes and incubated with 100 μg/mL and 200 μg/mL of LP, LPEx, and wEV for 24 h. Subsequently, the culture medium was replaced with a working solution prepared according to the instructions of the Calcein/PI cell viability and cytotoxicity assay kit (Beyotime, China). After incubating at 37 °C for 30 min, the cells were observed and recorded under a confocal microscope (FV3000, Olympus, Japan). The acquired images were analyzed using ImageJ software, and the percentage of living cells in each group was calculated as follows:

$$\text{Living cell}\ (\%) = \frac{\text{N}_\text{Lv}}{\text{N}_\text{Lv} + \text{N}_\text{D}} \times 100 \quad (5)$$

where N_{Lv} and N_D represent the number of living cells (green) and dead cells (red), respectively, in each image. Twenty images from each group were analyzed.

Lysosomal escape efficiency of LP, LPEx, and wEV

Following the methodology described above, Cy3-miR-NC was loaded separately using LP, LPEx, and wEV. They were then transfected into dermal fibroblasts and RAW267.4 cells at a concentration of 100 nM (Cy3-miR-NC). After 12 h, the culture medium was replaced with fresh medium, and the cells were further cultured for 24 h. Subsequently, the culture medium was removed from the culture dishes and replaced with a working solution prepared according to the instructions provided in the Lyso-Tracker Green assay kit (Beyotime, China). The cells were then incubated for 30 min, followed by observation and image capture using confocal microscopy. The obtained images were analyzed using ImageJ software, and the lysosome-escaping rate was calculated according to the following formula:

$$\text{Lysosome} - \text{escaping rate} = \frac{\text{A}_\text{m}}{\text{A}_\text{t}} \times 100 \quad (6)$$

where A_t represents the total fluorescence area of Cy3-miR-NC (red) in each image, and A_m indicates the fluorescence area of Cy3-miR-NC that does not colocalize with lysosomes (green). Twenty images from each group were analyzed.

Lysosomal escape kinetics of LPEx

The experimental procedure in this part was largely similar to the method described above. The difference was that after transfecting cells with LPEx loaded with Cy3-miR-NC for 12 h, the transfection medium was replaced

with fresh medium, and the cells were returned to the incubator for further culture. At subsequent time points of 6 h, 12 h, and 24 h, the cells were harvested, and the lysosomal escape rate was measured using the same method as described above.

Cell uptake mechanisms

Dermal fibroblasts and RAW267.4 cells were preincubated with different inhibitors for 30 min at 37 °C, including CPZ, amiloride, NaN_3, and nystatin (dissolved in normal saline, the concentrations were 0.6 mg/mL, 0.6 mg/mL, 0.5 mg/mL, and 2500 U/mL, respectively). The cells of the control group were treated with normal saline. After pretreatment, the cells were incubated with medium containing Cy3-miR-NC-loaded LPEx for 2 h. The cells were then washed twice with PBS and fixed with 4% paraformaldehyde for 10 min. DAPI was then added to stain the cell nuclei. The cellular uptake of LPEx was visualized using confocal microscopy. The obtained images were analyzed using ImageJ software, and the relative cell uptake degree of LPEx in each group was calculated according to the following formula:

$$\text{Relative cell uptake } (\%) = \frac{A_t}{A_{Ctl}} \times 100 \qquad (7)$$

where A_t represents the area of LPEx in the experimental group's image (red), and A_{Ctl} denotes the area of LPEx in the control group. Twenty images from each group were analyzed.

In vitro functional assessment of LPEx loaded with 28 miRNAs

Using the method described above, 28 miRNAs were encapsulated in LP, LPEx, and wEV to obtain LP-R, LPEx-R, and wEV-R, respectively. For dermal fibroblasts and macrophages, the transfection concentrations of miRNAs were 50 nM and 100 nM, respectively. In addition, $EX_{1.25}$ of 20 μg/mL and 40 μg/mL were applied to dermal fibroblasts and macrophages, respectively. LPExNC were also used to transfect dermal fibroblasts and macrophages at concentrations of 50 nM and 100 nM, respectively. The control and NC group cells were treated with regular culture medium. Cell proliferation assays, anti-inflammatory assays, and anti-fibrotic assays were performed following the methods described above.

In vivo functional assessment of LPEx-R on burn wounds

Deep second-degree burn wound preparation, wound size recording, and the time points of skin sample collection were all consistent with the methods described above. The difference lies in the injection administered to each group of mice, which consisted of either 20.0 μL of sterile PBS (control), 1.0 μg/μL (protein concentration) of $EX_{1.25}$, LPEx-R (loaded with 100 nM of miRNAs), or 100 nM of miRNAs loaded with HiPerFect transfection reagent. In addition, H&E staining was performed on wound tissue samples collected on days 6, 10, 14, and 18. Masson's staining was conducted on samples collected on days 10 and 14. Immunofluorescence staining for PCNA, IL-1β, and TNF-α was carried out on samples obtained on days 6 and 10, while α-SMA immunofluorescence staining was performed on samples collected on days 14 and 18.

Statistical analysis

Statistical analyses were performed using GraphPad Prism 10 (one-way ANOVA with Tukey's multiple comparison test) or Microsoft Excel (Student's t-test). Data were reported as mean ± standard deviation. $^{*}p < 0.05$, $^{**}p < 0.01$, $^{***}p < 0.001$, and $^{****}P < 0.0001$ were considered statistically significant.

Supplementary Information

The online version contains supplementary material available at https://doi.org/10.1186/s12951-025-03337-7.

Supplementary Material 1

Supplementary Material 2

Supplementary Material 3

Acknowledgements

The authors thank the Analytical and Testing Center of Huazhong University of Science and Technology, as well as the Research Core Facilities for Life Science (HUST), for their technical support.

Author contributions

Z.Y.L. conceived and designed the study, performed most of the experiments, and wrote the manuscript. X.J.C. performed part of the experiments and carried out data analysis. K.Z.C. and P.L. produced the figures and co-wrote the manuscript. M.Z.A. and L.G. reviewed, and edited the manuscript. L.J.Y. designed the study, supervised the research, reviewed, and edited the manuscript. All authors have approved the final version of the manuscript.

Funding

This study was supported by the Fundamental Research Funds for the Central Universities (grant numbers 2019kfyXKJC049 and 2023XCZX001) and the Hubei Engineering Research Center for both Edible and Medicinal Resources [grant number 2018BEC463]. The authors thank the extra financial support from Ezhou Ind Technol Res Inst, Ezhou 436060, China.

Data availability

No datasets were generated or analysed during the current study.

Declarations

Ethics approval and consent to participate

Animal experiments were approved by the Institutional Animal Care and Use Committee, Huazhong University of Science and Technology (IACUC Number: 3819). All surgeries were performed under anesthesia, and all efforts were made to minimize suffering.

Consent for publication

All authors have agreed to publish this article.

Competing interests
The authors declare no competing interests.

Author details
[1]Institute of Resource Biology and Biotechnology, Department of Biotechnology, College of Life Science and Technology, Huazhong University of Science and Technology, Wuhan 430074, China
[2]National Engineering Research Center for Nanomedicine, College of Life Science and Technology, Huazhong University of Science and Technology, Wuhan 430074, China
[3]Hubei Engineering Research Center for Both Edible and Medicinal Resources, Wuhan 430074, China

Received: 22 November 2024 / Accepted: 16 March 2025
Published online: 02 April 2025

References

1. Gerstl J, Kilgallon J, Nawabi N, Sinha I, Smith T, Pusic A, Subramanian SV, Ranganathan K. The global macroeconomic burden of burn injuries. Plast Reconstr Surg. 2021;9:159–60.
2. Wang Y, Beekman J, Hew J, Jackson S, Issler-Fisher AC, Parungao R, Lajevardi SS, Li Z, Mait PKM. Burn injury: Challenges and advances in burn wound healing, infection, pain and scarring. Adv Drug Deliv Rev. 2018;123:3–17.
3. Surowiecka A, Chrapusta A, Klimeczek-Chrapusta M, Korzeniowski T, Drukała J, Strużyna J. Mesenchymal stem cells in burn wound management. Int J Mol Sci. 2022;23:15339.
4. Zhang W, Ling Y, Sun Y, Xiao F, Wang L. Extracellular vesicles derived from mesenchymal stem cells promote wound healing and skin regeneration by modulating multiple cellular changes: A brief review. Genes. 2023;14:1516.
5. Marofi F, Alexandrovna KI, Margiana R, Bahramali M, Suksatan W, Abdelbasset WK, Chupradit S, Nasimi M, Maashi MS. MSCs and their exosomes: a rapidly evolving approach in the context of cutaneous wounds therapy. Stem Cell Res Ther. 2021;12:597.
6. Ahangar P, Mills SJ, Cowin AJ. Mesenchymal stem cell secretome as an emerging cell-free alternative for improving wound repair. Int J Mol Sci. 2020;21:7038.
7. Kimiz-Gebologlu I, Oncel SS, Exosomes. Large-scale production, isolation, drug loading efficiency, and biodistribution and uptake. J Control Release. 2022;347:533–43.
8. Chen J, Li P, Zhang T, Xu Z, Huang X, Wang R, Du L. Review on strategies and technologies for exosome isolation and purification. Front Bioeng Biotechnol. 2021;9:811971.
9. Yang Z, Shi J, Xie J, Wang Y, Sun J, Liu T, Zhao Y, Zhao X, Wang X, Ma Y, Malkoc V, Chiang C, Deng W, Chen Y, Fu Y, Kwak KJ, Fan Y, Kang C, Yin C, Rhee J, Bertani P, Otero J, Lu W, Yun K, Lee AS, Jiang W, Teng L, Kim BYS, Lee LJ. Large-scale generation of functional mRNA-encapsulating exosomes via cellular nanoporation. Nat Biomed Eng. 2020;4:69–83.
10. Aday S, Halevy I, Anwar M, Madeddu P, Sahoo S, Petretto E, Dan P, Emanueli C. Development of bioinspired synthetic exosomes with proangiogenic potential. Circ Res. 2019;125:A130.
11. Mondal J, Pillarisetti S, Junnuthula V, Saha M, Hwang SR, Park I, Lee Y. Hybrid exosomes, exosome-like nanovesicles and engineered exosomes for therapeutic applications. J Control Release. 2023;353:1127–49.
12. Liu J, Sun Y, Zeng X, Liu Y, Liu C, Zhou Y, Liu Y, Sun G, Guo M. Engineering and characterization of an artificial drug-carrying vesicles nanoplatform for enhanced specifically targeted therapy of glioblastoma. Adv Mater. 2023;35:e2303660.
13. Shang R, Lee S, Senavirathne G, Lai EC. MicroRNAs in action: biogenesis, function and regulation. Nat Rev Genet. 2023;24:816–33.
14. DeVeale B, Swindlehurst-Chan J, Blelloch R. The roles of microRNAs in mouse development. Nat Rev Genet. 2021;22:307–23.
15. Cunha E, Rocha K, Ying W, Olefsky JM. Exosome-mediated impact on systemic metabolism. Annu Rev Physiol. 2024;86:225–53.
16. Agbu P, Carthew RW. MicroRNA-mediated regulation of glucose and lipid metabolism. Nat Rev Mol Cell Biol. 2021;22:425–38.
17. Inui M, Martello G, Piccolo S. MicroRNA control of signal transduction. Nat Rev Mol Cell Biol. 2010;11:252–63.
18. Zhai M, Zhu Y, Yang M, Mao C. Human mesenchymal stem cell derived exosomes enhance cell-free bone regeneration by altering their miRNAs profiles. Adv Sci. 2020;7:2001334.
19. Meng Z, Zhou D, Gao Y, Zeng M, Wang W. MiRNA delivery for skin wound healing. Adv Drug Deliv Rev. 2018;129:308–18.
20. Peng B, Chen Y, Leong KW. MicroRNA delivery for regenerative medicine. Adv Drug Deliv Rev. 2015;88:108–22.
21. Zhang X, Sai B, Wang F, Wang L, Wang Y, Zheng L, Li G, Tang J, Xiang J. Hypoxic BMSC-derived exosomal miRNAs promote metastasis of lung cancer cells via STAT3-induced EMT. Mol Cancer. 2019;18:40.
22. Zhang Y, Kim MS, Jia B, Yan J, Zuniga-Hertz JP, Han C, Cai D. Hypothalamic stem cells control ageing speed partly through exosomal miRNAs. Nature. 2017;548:52–7.
23. Bogdanowicz DR, Lu HH. Designing the stem cell microenvironment for guided connective tissue regeneration. Ann N Y Acad Sci. 2017;1410:3–25.
24. Freytes DO, Kang JW, Campos IM, Novakovic GV. Macrophages modulate the viability and growth of human mesenchymal stem cells. J Cell Biochem. 2013;114:220–29.
25. Vallés G, Bensiamar F, Maestro-Paramio L, García-Rey E, Vilaboa N, Saldaña L. Influence of inflammatory conditions provided by macrophages on osteogenic ability of mesenchymal stem cells. Stem Cell Res Ther. 2020;11:57.
26. Jeschke MG, Wood FM, Middelkoop E, Bayat A, Teot L, Ogawa R, Gauglitz GG. The scars. Nat Rev Dis Primers. 2023;9:64.
27. Li M, Wang M, Wen Y, Zhang H, Zhao G, Gao Q. Signaling pathways in macrophages: molecular mechanisms and therapeutic targets. MedComm. 2023;4:e349.
28. Minakawa T, Yamashita JK. Extracellular vesicles and microRNAs in the regulation of cardiomyocyte differentiation and proliferation. Arch Biochem Biophys. 2023;749:109791.
29. Ouyang Z, Wei K. MiRNA in cardiac development and regeneration. Cell Regeneration. 2021;10:14.
30. Yin J, Zhang S, Yang C, Wang Y, Shi B, Zheng Q, Zeng H. Mechanotransduction in skin wound healing and scar formation: Potential therapeutic targets for controlling hypertrophic scarring. Front Immunol. 2022;13:1028410.
31. Wu X, He W, Mu X, Liu Y, Deng J, Liu Y, Nie X. Macrophage polarization in diabetic wound healing. Burns Trauma. 2022;10:tkac051.
32. Xu Z, Dong M, Yin S, Dong J, Zhang M, Tian R, Min W, Zeng L, Qiao H, Chen J. Why traditional herbal medicine promotes wound healing: Research from immune response, wound microbiome to controlled delivery. Adv Drug Deliv Rev. 2023;195:114764.
33. Finnerty CC, Jeschke MG, Branski LK, Barret JP, Dziewulski P, Herndon DN. Hypertrophic scarring: the greatest unmet challenge after burn injury. Lancet. 2016;388:1427–36.
34. Ruseska I, Zimmer A. Cellular uptake and trafficking of peptide-based drug delivery systems for miRNA. Eur J Pharm Biopharm. 2023;191:189–204.
35. Bunggulawa EJ, Wang W, Yin T, Wang N, Durkan C, Wang Y, Wang G. Recent advancements in the use of exosomes as drug delivery systems. J Nanobiotechnol. 2018;16:81.
36. Kalluri R, LeBleu VS. The biology, function, and biomedical applications of exosomes. Science. 2020;367:eaau6977.
37. Xu X, Yuan T, Dad HA, Shi M, Huang Y, Jiang Z, Peng L. Plant exosomes as novel nanoplatforms for microRNA transfer stimulate neural differentiation of stem cells in vitro and in vivo. Nano Lett. 2021;21:8151–59.
38. Cong M, Tan S, Li S, Gao L, Huang L, Zhang H, Qiao H. Technology insight: Plant-derived vesicles—How far from the clinical biotherapeutics and therapeutic drug carriers? Adv Drug Deliver Rev. 2022;182:114108.
39. Yang L, Zhao Q, Guo Z, Liu Y, Gao W, Pu Y, He B. Konjac glucomannan hydrogel dressing and its combination with Chinese medicine for the wound treatment. New J Chem. 2022;46:2377–87.
40. Hu G, Liu W, Li L. Identification and quantification of cucurbitacin in watermelon frost using molecular networking integrated with ultra-high-performance liquid chromatography-tandem mass spectrometry. J Sep Sci. 2023;46:2300019.
41. Lin Z, Long F, Kang R, Klionsky DJ, Yang M, Tang D. The lipid basis of cell death and autophagy. Autophagy. 2024;20:469–88.
42. Fang Z, Liu K. Plant-derived extracellular vesicles as oral drug delivery carriers. J Control Release. 2022;350:389–400.
43. Tsakiri M, Tsichlis I, Zivko C, Demetzos C, Mahairaki V. Lipidic nanoparticles, extracellular vesicles and hybrid platforms as advanced medicinal products: future therapeutic prospects for neurodegenerative diseases. Pharmaceutics. 2024;16:350.
44. Capriglione F, Verrienti A, Celano M, Maggisano V, Sponziello M, Pecce V, Gagliardi A, Giacomelli L, Aceti V, Durante C, Bulotta S, Russo D. Analysis of serum microRNA in exosomal vehicles of papillary thyroid cancer. Endocrine. 2022;75:185–93.

45. Aziz MA, Seo B, Hussaini HM, Hibma M, Rich AM. Comparing two methods for the isolation of exosomes. J Nucleic Acids. 2022, 8648373.
46. Sun M, Yang J, Fan Y, Zhang Y, Sun J, Hu M, Sun K, Zhang J. Beyond extracellular vesicles: Hybrid membrane nanovesicles as emerging advanced tools for biomedical applications. Adv Sci. 2023;10:303617.
47. Caracciolo G. Liposome–protein corona in a physiological environment: Challenges and opportunities for targeted delivery of nanomedicines. Nanomedicine: NBM. 2015;11:543–57.
48. Onishchenko N, Tretiakova D, Vodovozova E. Spotlight on the protein corona of liposomes. Acta Biomater. 2021;134:57–78.
49. Sun M, Yuan Y, Lu F, Di Pasqua AJ. Physicochemical factors that influence the biocompatibility of cationic liposomes and their ability to deliver DNA to the nuclei of ovarian cancer SK-OV-3 cells. Materials. 2021;14:416.
50. Canton I, Battaglia G. Endocytosis at the nanoscale. Chem Soc Rev. 2012;41:2718–39.
51. Smith SA, Selby LI, Johnston APR, Such GK. The endosomal escape of nanoparticles: Toward more efficient cellular delivery. Bioconjug Chem. 2019;30:263–72.
52. Zhou Z, Li H, Wang K, Guo Q, Li C, Jiang H, Hu Y, Oupicky D, Sun M. Bioreducible cross-linked hyaluronic acid/calcium phosphate hybrid nanoparticles for specific delivery of siRNA in melanoma tumor therapy. ACS Appl Mater Inter. 2017;9:14576–89.
53. Hamzah RN, Alghazali KM, Biris AS, Griffin RJ. Exosome traceability and cell source dependence on composition and cell-cell cross talk. Int J Mol Sci. 2021;22:5346.
54. Rodrigues JP, Da Costa Silva JR, Ferreira BA, Veloso LI, Quirino LS, Rosa RR, Barbosa MC, Rodrigues CM, Gaspari PBF, Beletti ME, Goulart LR, Corrêa NCR. Development of collagenous scaffolds for wound healing: characterization and in vivo analysis. J Mater Sci Mater Med. 2024;35:12.
55. Zhou CJ, Guo Y. Mini review on collagens in normal skin and pathological scars: current understanding and future perspective. Front Med. 2024;11:1449597.
56. Moldovan GL, Pfander B, Jentsch S. PCNA, the maestro of the replication fork. Cell. 2007;129:665–79.
57. Jones RT, Smith KL. The role of PCNA in wound healing: From cell proliferation to tissue remodeling. Nat Rev Mol Cell Biol. 2020;21:589–604.
58. Eming SA, Krieg T, Davidson JM. Inflammation in wound repair: Molecular and cellular mechanisms. J Invest Dermatol. 2007;127:514–25.
59. Emiliani C. Plant-derived extracellular vesicles: Natural nanocarriers for biotechnological drugs. Processes. 2024, 12.
60. Nakano M, Nagaishi K, Konari N, Saito Y, Chikenji T, Mizue Y, Fujimiya M. Bone marrow-derived mesenchymal stem cells improve diabetes-induced cognitive impairment by exosome transfer into damaged neurons and astrocytes. Sci Rep. 2016;6:24805.
61. Rittié L. Type I collagen purification from rat tail tendons. Methods Mol Biol. 2017;1627:287–308.
62. Chen S, Zhou Y, Chen Y, Gu J, Fastp. An ultra-fast all-in-one FASTQ preprocessor. Bioinformatics. 2018;34:i884–90.
63. Kozomara A, Griffiths-Jones S, miRBase. Annotating high confidence microRNAs using deep sequencing data. Nucleic Acids Res. 2014;42:D68–73.
64. An J, Lai J, Lehman ML, Nelson CC. miRDeep: An integrated application tool for miRNA identification from RNA sequencing data. Nucleic Acids Res. 2013;41:727–37.
65. Enright A, John B, Gaul U, TuschI T, Sander C, Marks D. MicroRNA targets in Drosophila. Genome Biol. 2003;5:R1.
66. Krüger J, Rehmsmeier M. RNAhybrid: microRNA target prediction easy, fast and flexible. Nucleic Acids Res. 2006;34:W451–4.
67. Agarwal V, Bell GW, Nam J, Bartel DP. Predicting effective microRNA target sites in mammalian mRNAs. Elife. 2015;4:e5005.
68. Alvarez-Erviti L, Seow Y, Yin H, Betts C, Lakhal S, Wood MJA. Delivery of siRNA to the mouse brain by systemic injection of targeted exosomes. Nat Biotechnol. 2011;29:341–5.

Publisher's note